This manuscript is a pre-copyedited, author-produced PDF of an article accepted for publication in *Geophysical Journal International* following peer review. The version of record of ”Revisiting the 2015 Mw=8.3 Illapel earthquake: Unveiling complex fault slip properties using Bayesian inversion.” will be available online at: doi:10.1093/gji/ggad380.

submitted to *Geophys. J. Int.*

Revisiting the 2015 Mw=8.3 Illapel earthquake: Unveiling complex fault slip properties using Bayesian inversion.

E. Caballero[1,2], Z. Duputel[1,4], C. Twardzik[1,10], L. Rivera[1], E. Klein[3], J. Jiang[5], C. Liang[6], L. Zhu[7], R. Jolivet[3,8], E. Fielding[9], M. Simons[7]

[1] *Institut Terre et Environment de Strasbourg, UMR 7063, Université de Strasbourg/EOST, CNRS, Strasbourg, France.*

[2] *Institut des Sciences de la Terre, UMR 5275, Université de Grenoble-Alpes, CNRS, Grenoble, France*

[3] *Laboratoire de Géologie, Département de Géosciences, École Normale Supérieure, PSL Université, CNRS UMR 8538, Paris, France.*

[4] *Observatoire Volcanologique du Piton de La Fournaise Institut de Physique du Globe de Paris.*

[5] *University of Oklahoma Norman Campus, School of Geosciences, Norman, OK, United States.*

[6] *Institute of Remote Sensing and Geographic Information System, Peking University, Beijing, China.*

[7] *Seismological Laboratory, California Institute of Technology, Pasadena, CA, United States.*

[8] *Institut Universitaire de France, 1 rue Descartes, 75005 Paris, France.*

[9] *Jet Propulsion Laboratory, California Institute of Technology, Pasadena, CA, United States.*

[10] *Université Côte d'Azur, CNRS, Observatoire de la Côte d'Azur, IRD, Geoazur, UMR 7329, Valbonne, France.*

Received 2023 March 30

SUMMARY

The 2015 moment magnitude $M_W = 8.3$ Illapel earthquake is the largest mega-thrust earthquake that has been recorded along the Chilean subduction zone since the 2010 $M_W = 8.8$ Maule earthquake. Previous studies indicate a rupture propagation from the hypocenter to shallower parts of the fault, with a maximum slip varying from 10 to 16 meters. The amount of shallow slip differs dramatically between rupture models with some results showing almost no slip at the trench and other models with significant slip at shallow depth. In this work, we revisit this event by combining a comprehensive data set including continuous and survey

GNSS data corrected for post-seismic and aftershock signals, ascending and descending InSAR images of the Sentinel-1A satellite, tsunami data along with high-rate GPS, and doubly integrated strong-motion waveforms. We follow a Bayesian approach, in which the solution is an ensemble of models. The kinematic inversion is done using the cascading capability of the AlTar algorithm, allowing us to first get a static solution before integrating seismic data in a joint model. In addition, we explore a new approach to account for forward problem uncertainties using a second-order perturbation approach. Results show a rupture with two main slip patches, with significant slip at shallow depth. During the rupture propagation, we observe two regions that are encircled by the rupture, with no significant slip, westward of the hypocenter. These encircling effects have been previously suggested by back-projection results but have not been observed in finite-fault slip models. We propose that the encircled regions correspond to regions where the yield stress largely exceeds the initial stress or regions where fracture energy is too large to be ruptured during earthquakes such as the Illapel one. These asperities may potentially break in the future and probably already broke in the past.

Key words: Inverse theory; Probability distributions; Earthquake source observations.

1 INTRODUCTION

Chile is one of the most seismically active regions on Earth, where the Nazca plate subducts under the South American plate with a convergence rate of approximately 67 mm/yr (Angermann et al. 1999; Vigny et al. 2009). This large plate convergence rate is accomodated in parts by the occurrence of large megathrust earthquakes, such as the 1943 moment magnitude $M_W = 7.9 - 8.3$ Illapel event, the 1960 $M_W = 9.5$ Valdivia earthquake, the 2010 $M_W = 8.8$ Maule earthquake, and the 2014 $M_W = 8.1$ Iquique earthquake (Lomnitz 2004; Ruiz & Madariaga 2018). The latest megathrust earthquake in Chile is the 2015 $M_W = 8.3$ Illapel earthquake, which occurred off the west coast of the Coquimbo region on September 16th, 2015, at 22:54:31 UTC (Centro Sismológico Nacional, CSN) (Li et al. 2016; Ruiz & Madariaga 2018). The 2015 Illapel earthquake initiated at a depth of 23 km and triggered a trans-pacific tsunami with waves reaching more than 4 meters high in Chile (An & Meng 2017; Fernández et al. 2019). The thrust focal mechanism is consistent with the rupture of the megathrust interface (Ekström et al. 2012). Most source inversions suggested that the rupture lasted around 100 seconds (Heidarzadeh et al. 2016; Melgar et al. 2016; Tilmann et al. 2016) but some studies report much larger rupture durations (e.g., Lee et al. 2016). The previous earthquake to rupture this section of the megathrust occurred in 1943, with a smaller magnitude between $M_W = 7.9 - 8.3$, and a duration of approximately 30 seconds (Beck et al. 1998; Lomnitz 2004; Ruiz & Madariaga 2018). The hypocentral depth of the 1943 event is unfortunately not well resoved and is estimated between 10 and 30 km.

Different groups have published kinematic slip rupture models for the 2015 $M_W = 8.3$ Illapel earthquake. As discussed by Satake & Heidarzadeh (2017), even though all of these models share general features, some properties of the rupture are still under debate (An & Meng 2017; Heidarzadeh et al. 2016; Li et al. 2016; Ruiz et al. 2016; Tilmann et al. 2016; Williamson et al. 2017). For example, An & Meng (2017) suggest the absence of shallow slip, while other studies indicate that shallow slip is necessary to explain tsunami records (Lay et al. 2016; Li et al. 2016; Tilmann et al. 2016). In fact, Tilmann et al. (2016) suggested that the 1943 and 2015 events differ in their shallow slip.

The degree of rupture complexity also varies among previously published results. In contrast with the relatively simple rupture processes suggested by the aforementioned results, other studies suggest a more complex rupture scenario with at least two main slip asperities (Melgar et al. 2016; Lee et al. 2016). While the relatively compact model of Melgar et al. (2016) is consistent with tsunami observations, Lay et al. (2016) show that the model of Lee et al. (2016) involving a broad area of shallow slip rupturing multiple times cannot reproduce tsunami data. Several back-projections studies confirm the complexity of the 2015 Illapel rupture (Melgar et al. 2016; Okuwaki et al. 2016; Yin et al. 2016). A common result among back-projection studies is that the Illapel earthquake presents a northwestward migration. For example, An et al. (2017) shows a complex frequency dependent rupture propagation with several branches. The back-projected low-frequency (LF) sources migrate mainly updip to the west, while the high-frequency (HF) sources initially move down-dip toward the northeast before veering up-dip towards the northwest. On the other hand, Meng et al. (2018) suggest a rupture that splits into two different branches separated along dip. The analysis of these multiple rupture branches suggests an encircling rupture that seems to be aligned with regions experiencing a high slip rate and large shallow slip. Unfortunately, such a complex pattern hasn't been confirmed by kinematic slip inversion models yet. Potentially, such encircling rupture effect is only constrained by the high-frequency wavefield, hence not resolvable with slip inversions. In addition, such encircling pattern likely involves abrupt changes in rupture velocities, while most slip inversions consider fixed rupture velocities and smoothing constraints.

In this work, we revisit the 2015 $M_W = 8.3$ Illapel earthquake by combining a comprehensive data set including permanent and survey GPS stations corrected for post-seismic and aftershock signals, ascending and descending Sentinel-1A InSAR images along with high-rate GPS and doubly integrated strong-motion waveforms. We follow a Bayesian approach using the AlTar code, which allows us to obtain the posterior probability distribution of slip models rather than a single optimum solution. We also employ a non-linear parameterization enabling significant variation of rupture velocity during the rupture process. We also analyze the impact that prediction error covariance matrices have on coseismic slip inversions results.

2 DATA

We investigate the complex rupture of the 2015 $M_W = 8.3$ Illapel earthquake using multiple datasets that are shown in Figure 1. This database includes GPS offsets, Interferometric Synthetic Aperture Radar (InSAR) images, tsunami data along with high-rate GPS and strong motion waveforms.

InSAR images are obtained from the Sentinel-1A satellite with ascending and descending orbits (see text S1). We use 14 tsunami stations: 6 DART buoys and 6 coast gauges focusing mainly on first arrivals and open sea sites to minimize coastal effects (see text S2). We use daily and survey GPS data provided by Klein et al. (2017). Both datasets are affected by co-seismic offsets induced by $M_W = 7.1$ and $M_W = 6.8$ aftershocks occurring respectively 23 min and 5 hours after the mainshock. Survey GPS data also includes several weeks of post-seismic displacement. Details of GPS data processing can be found in Klein et al. (2017). To correct both daily and campaign GPS data from aftershocks and post-seismic deformation, we use high-rate post-seismic time-series from Twardzik et al. (2021). These measurements are spatially interpolated using cubic splines and removed from co-seismic GPS offsets. We estimate uncertainty associated with the corrected data by conducting the aforementioned correction stochastically (using Gaussian realizations given uncertainties on daily, survey and post-seismic GPS datasets). A comparison between corrected and uncorrected GPS data is shown in Figure A1. We note that the nominal standard deviations of the GPS data are unrealistically small (i.e. on the order of 5-10 mm), leading to overfitting of the GPS coseismic displacements in the inversion procedure. To mitigate this issue, we scale the resulting standard deviations to ensure a unit reduced χ^2_ν, a statistical indicator that helps to correct for over or under estimation of uncertainties (supplementary information text S3). As a result, we increase the standard deviation of the GPS static displacements by a factor of 10 for the East component and 5 for the North and Vertical components. While this approach is empirical, it allows us to avoid any overfitting of the GPS observations while keeping a relative weighting between stations based on the variability of the corrected observations.

For the kinematic data set (i.e., seismic waveforms), we use records from High Rate GPS (HRGPS) stations and strong motion data located within 5 degrees from the mainshock hypocenter. These stations are part of the Chilean Seismological Service (CSN) of the Universidad de Chile (Universidad de Chile 2012). In total, we have 96 strong motion waveforms that we double integrate into displacement time series and 12 HRGPS components. The integration of acceleration data is a delicate operation that can easily result in large drifts in velocity and displacement waveforms. Therefore, to obtain displacement records, after removing any linear trend in accelerograms, we remove an additional velocity drift at the end of the waveforms. This additional coda correction is done by using a quadratic function to fit displacement waveforms from the time when 90% of the acceleration energy is reached. Visual inspection of the corrected displacement records is then done to ensure the good quality of the data. To further check the corrected records, we compare the obtained strong motion displacements with HRGPS displacements (Figure 2 and Figure A2). In total, we were able to recover 43 displacement components from strong motion with high-quality displacement waveforms.

To calculate synthetic static displacements, we use the Classic Slip Inversion (CSI) package

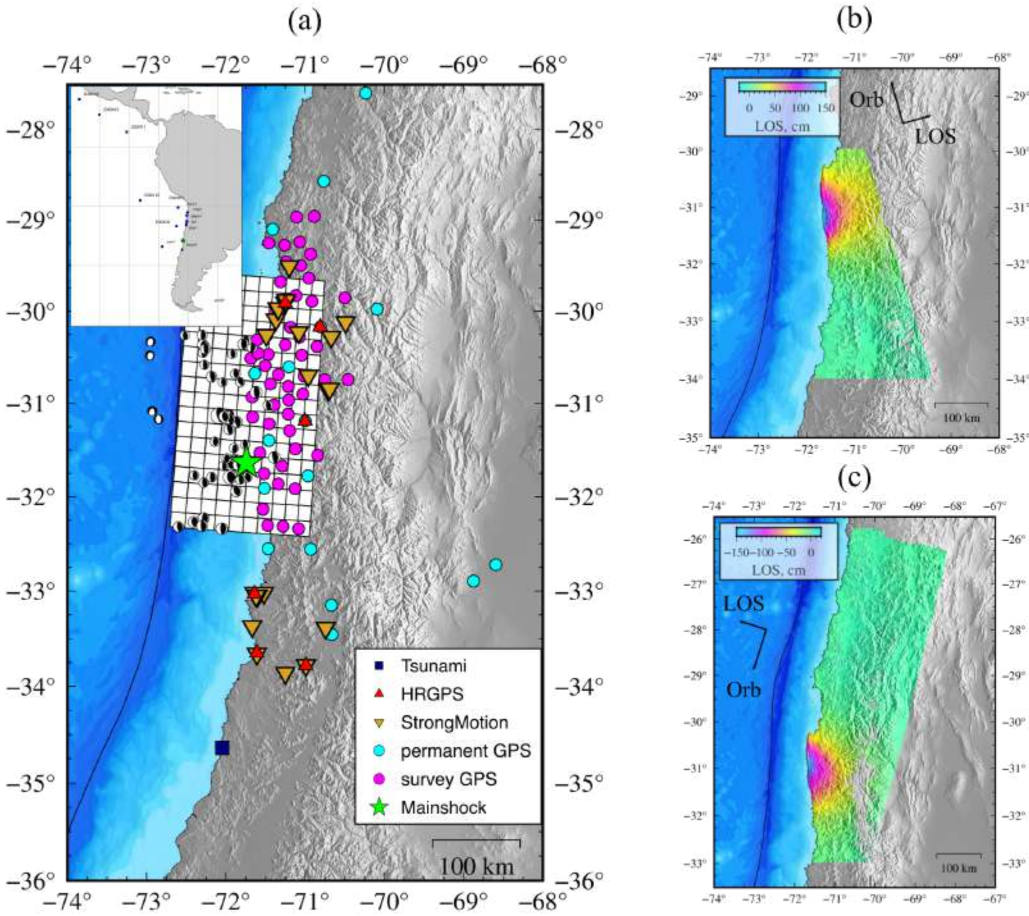

Figure 1. General overview of the studied region with data sets used in this study (a). Green star represents the hypocenter obtained by the Chilean Seismological Center (CSN). White rectangles represent the fault geometry used in this study. Focal mechanisms correspond to aftershocks Global CMT solutions. Ascending (b) and descending (c) Sentinel-1A InSAR images. Small black arrows represent the LOS and orbit direction, respectively.

(`https://github.com/jolivetr/csi`), using the approach of Zhu & Rivera (2002) for a layered Earth model. We calculate Green's Functions using the one-dimensional velocity model built by Duputel et al. (2015) (see Figure 3). For the kinematic Green's Functions, we use the wavenumber integration code of the CPS seismology package (`http://www.eas.slu.edu/eqc/eqccps.html`) from (Herrmann 2013). We filter both the kinematic Green's function and data in the 0.01 - 0.06667 Hz passband.

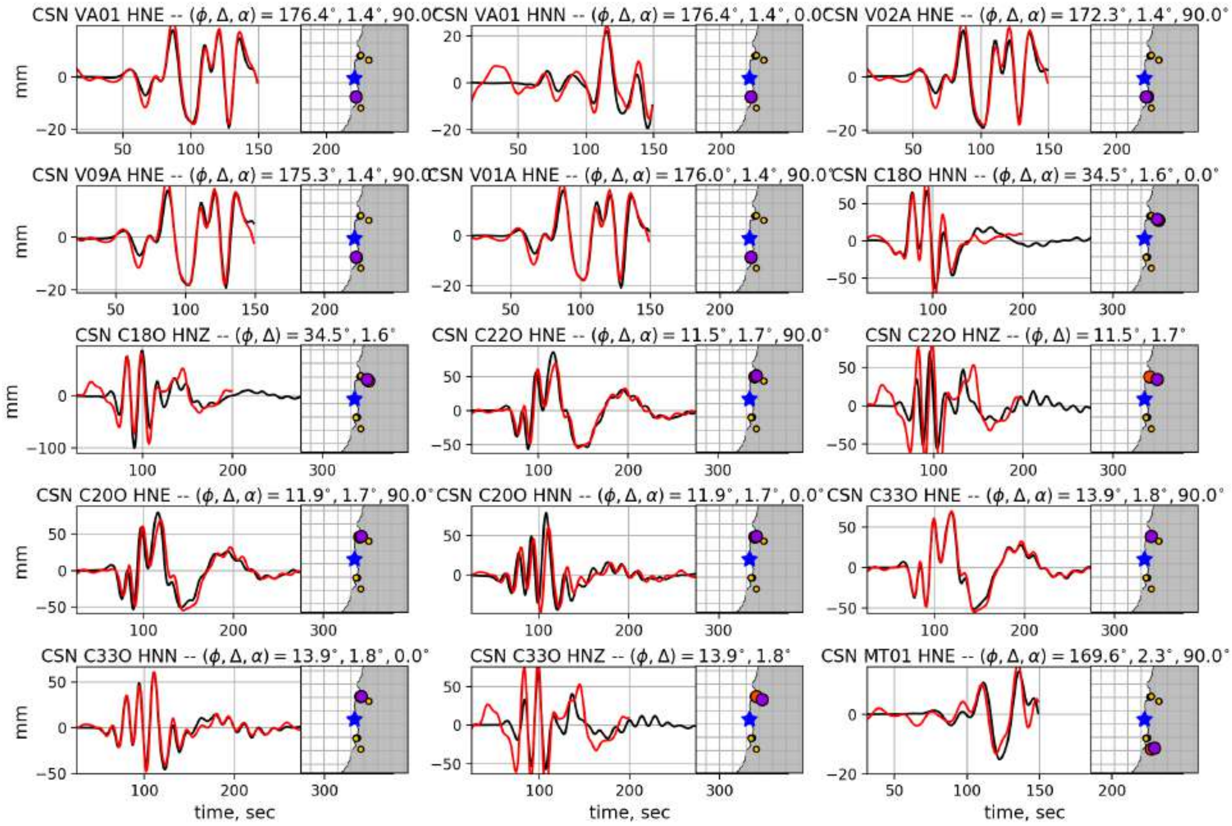

Figure 2. Comparison between displacements corrected from strong motion records and HRGPS displacements. Red and black waveforms represent HRGPS and strong motion respectively. On the maps, the blue star represents the CSN hypocenter while circles indicate station location (orange for the strong motion station considered, yellow for the other strong motion stations, and purple for HRGPS stations). ϕ, and Δ represent the azimuth and distance from the epicenter. The angle α is the component azimuth (0° -north, 90° -east). Time-shifts between waveforms are due to slight differences in station location (i.e., between HRGPS and strong motion records). Other examples of comparison are shown in Figure A2.

3 METHODOLOGY

To perform the inversion, we follow a Bayesian approach in which we obtain an ensemble of models and not a unique solution. The inversion is done using the cascading capability of the AlTar code (`https://altar.readthedocs.io`), allowing us to first get a static solution, and then to integrate waveform data in a joint model. This code is based on the Cascading Adaptative Metropolis In Parallel (CATMIP) algorithm proposed by Minson et al. (2013) that we will describe below. The AlTar package has been successfully employed for different problems. Jolivet et al. (2015), Jolivet et al. (2020) and Jolivet et al. (2023) estimated the interseismic coupling of the San

Andreas fault, the Northern Chile subduction interface and the North Anatolian fault. Studies of individual earthquakes have been carried out by Duputel et al. (2015), Bletery et al. (2016), and Gombert et al. (2018a), among others.

Starting from Bayes theorem, we write the *a posteriori* probability density function (PDF) of the parameters $\mathbf{m}$, given the observations $\mathbf{d_{obs}}$:

$$p(\mathbf{m}|\mathbf{d_{obs}}) = \kappa \, p(\mathbf{m}) \, p(\mathbf{d_{obs}}|\mathbf{m}), \tag{1}$$

where $p(\mathbf{m})$ is the *a priori* probability density function of parameters, $p(\mathbf{d_{obs}}|\mathbf{m})$ is the data likelihood function and κ a normalization factor. We define the likelihood function as:

$$p(\mathbf{d_{obs}}|\mathbf{m}) = \mathbf{exp}\left(-\frac{\mathbf{1}}{\mathbf{2}}(\mathbf{d_{obs}} - \mathbf{g(m)})^{\mathbf{T}}\mathbf{C}_{\chi}{}^{\mathbf{-1}}(\mathbf{d_{obs}} - \mathbf{g(m)})\right). \tag{2}$$

$\mathbf{C}_\chi$ is the misfit covariance matrix that is the sum of $\mathbf{C_d}$ and $\mathbf{C_p}$, which correspond to covariance matrices describing observational and forward modeling uncertainties, respectively. We sample the *a posteriori* PDF using a series of transitional intermediate PDF. The transitional PDFs are controlled by the tempering parameter β, which modulates the information content at each transitional step such as:

$$f(\mathbf{m}|\mathbf{d_{obs}}, \beta_{\mathbf{k}}) = \kappa \, p(\mathbf{m}) \, p(\mathbf{d_{obs}}|\mathbf{m})^{\beta_{\mathbf{k}}}, \tag{3}$$

where $(k = 1, \ldots, M)$ and β varies from zero to one, i.e., $0 = \beta_0 < \beta_1, \ldots, \beta_M = 1$.

These transitional steps will converge to the final solution by smoothly informing the system (i.e., by increasing β). In addition, we apply a cascading approach to improve the convergence of the sampler by first solving for the static problem before sampling the full joint kinematic slip inversion. More details about the algorithm can be found in Minson et al. (2013). As mentioned before, the $\mathbf{C}_\chi$ matrix incorporates different uncertainty assessments. The observational uncertainty is commonly related to errors in measurements. The details of observational uncertainty estimates can be found in text S4.

Prediction uncertainties are associated with imperfect forward modelling that can be caused by different factors, such as imperfect Earth models or fault geometries (Beresnev 2003; Ide 2015; Wald & Graves 2001; Williams & Wallace 2015). Several studies have highlighted the importance of considering forward modeling uncertainties in slip inversions (Duputel et al. 2012, 2014; Hallo

& Gallovič 2016; Ragon et al. 2018; Yagi & Fukahata 2011). For example, Duputel et al. (2014) study the uncertainties linked to inaccuracies in the Earth structure model. On the other side, Ragon et al. (2018) analyze uncertainties associated with inaccuracies in fault geometries. Also, Razafindrakoto & Mai (2014) assess the influence of the employed source time function and elastic structure on earthquake slip imaging.

In the present study, we focus on accounting uncertainties due to Earth structure modeling. Specifically, we evaluate the impact of inaccuracies in the 1D velocity model employed to compute static and kinematic predictions. Uncertainties in the elastic parameters $\mathbf{\Psi}$ is assumed to follow a log-normal distribution:

$$p(log\ \mathbf{\Psi}) = \frac{1}{\sqrt{(2\pi)^N |\mathbf{C_\Psi}|}} \exp\left(-\frac{1}{2}(\log\mathbf{\Psi} - \log\tilde{\mathbf{\Psi}})^T \mathbf{C_\Psi}(\log\mathbf{\Psi} - \log\tilde{\mathbf{\Psi}})\right), \qquad (4)$$

where $\mathbf{C_\Psi}$ is the covariance characterizing uncertainty around $\log\tilde{\mathbf{\Psi}}$ (the logarithm of the elastic parameters used to compute the predictions shown in Figure 3). This choice of a log-normal distribution is motivated by the fact that (1) the elastic parameters are strictly positive and (2) $\mathbf{\Psi}$ values are derived from tomography techniques based on relative model perturbations ($\delta\log\mathbf{\Psi}$; (e.g., Tromp et al. 2005)). The Earth model uncertainty considered in the present study is shown in Figure 3. This level of variability is measured by comparing different models from the region (following Duputel et al. 2015).

We follow three different schemes to map Earth model uncertainty into prediction uncertainty. The first straightforward approach is to empirically calculate the prediction uncertainty covariance matrix $\mathbf{C_p}$ using predictions computed for a large number of random Earth models $\mathbf{\Psi^i}, (i = 1, \ldots, n)$ drawn from $p(\log\mathbf{\Psi})$:

$$\mathbf{C_p} = \frac{1}{n-1}\sum_{i=1}^{n}(\mathbf{g}(\mathbf{\Psi^i},\mathbf{m}) - \mathbf{g}(\tilde{\mathbf{\Psi}},\mathbf{m}))\ (\mathbf{g}(\mathbf{\Psi^i},\mathbf{m}) - \mathbf{g}(\tilde{\mathbf{\Psi}},\mathbf{m}))^T, \qquad (5)$$

where $\mathbf{g}(\mathbf{\Psi^i},\mathbf{m})$ is the prediction for the Earth model $\mathbf{\Psi^i}$ and the source model $\mathbf{m}$. In our case, we use a preliminary source model $\mathbf{m}$ derived from a first preliminary slip inversion. $\mathbf{g}(\tilde{\mathbf{\Psi}},\mathbf{m})$ is the prediction response for the average Earth model $\tilde{\mathbf{\Psi}}$. This empirical approach is computationally expensive because it needs the calculation of predictions for each randomly generated Earth model. To evaluate the number of models $\mathbf{n}$ necessary to calculate an accurate empirical $\mathbf{C_p}$ matrix, we

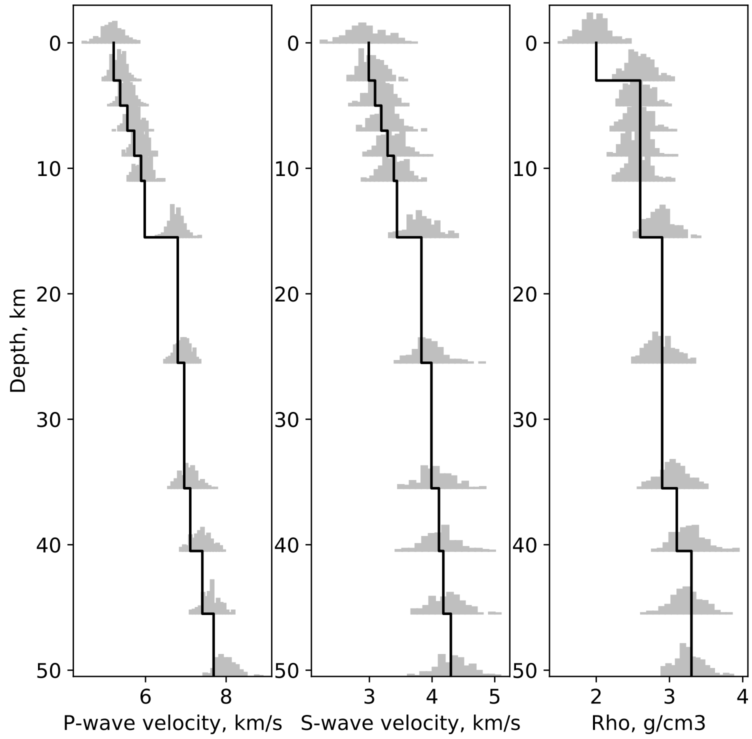

Figure 3. Model variability of the P-wave, S-wave, and density as a function of depth in the Illapel region. The black line represents the velocity layered model used for Green's Function (GF) calculation. Grey histograms are the probability density function for each parameter as a function of depth.

compare empirical $\mathbf{C_p}$ matrices calculated for an increasing number of random Earth models. We observe that the empirical $\mathbf{C_p}$ matrix is converging using 195 random Earth samples (Figure A3), corresponding to relatively smooth histograms in Figure 3.

To test a computationally less expensive approach, we also follow the first-order approximation approach proposed by Duputel et al. (2014). Assuming that we can approximate our forward model $\mathbf{g}(\mathbf{\Psi}, \mathbf{m})$ by linearized perturbations, for an *a priori* Earth model we have then:

$$\mathbf{g}(\mathbf{\Psi}, \mathbf{m}) \approx \mathbf{g}(\tilde{\mathbf{\Psi}}, \mathbf{m}) + \mathbf{K_\Psi}(\tilde{\mathbf{\Psi}}, \mathbf{m}) \cdot (\mathbf{\Psi} - \tilde{\mathbf{\Psi}}), \tag{6}$$

where $\mathbf{K}$ is the sensitivity kernels of the prediction with respect to elastic parameters used to compute forward predictions:

$$(\mathbf{K_\Psi})_{ij}(\tilde{\mathbf{\Psi}}, \mathbf{m}) = \frac{\partial g_i}{\partial \Psi_j}(\tilde{\mathbf{\Psi}}, \mathbf{m}), \tag{7}$$

where Ψ_j corresponds to the j-th elastic parameter in the Earth model $\mathbf{\Psi}$. We use then $\mathbf{K}$ to estimate $\mathbf{C_p}$ as:

$$\mathbf{C_p} = \mathbf{K_\Psi} \cdot \mathbf{C_\Psi} \cdot \mathbf{K_\Psi^T}, \tag{8}$$

where $\mathbf{C_\Psi}$ is the same log-normal covariance that we use for perturbating the random models of the empirical $\mathbf{C_p}$ in equation 4. While this approach looks appropriate for static data, it could be problematic for kinematic data as the link between Earth model perturbations and waveform predictions is probably not linear. Indeed, changes in the velocity model induce both time-shifts and amplitude variations in the predicted waveforms.

Therefore, we also explore the possibility of using a 2nd order perturbation approach of the forward model as:

$$\mathbf{g}(\mathbf{\Psi}, \mathbf{m}) \approx \mathbf{g}(\tilde{\mathbf{\Psi}}, \mathbf{m}) + \mathbf{K_\Psi}(\tilde{\mathbf{\Psi}}, \mathbf{m}) \cdot (\mathbf{\Psi} - \tilde{\mathbf{\Psi}}) + \frac{1}{2}\,(\mathbf{\Psi} - \tilde{\mathbf{\Psi}}) \cdot \mathbf{H_\Psi}(\tilde{\mathbf{\Psi}}, \mathbf{m}) \cdot (\mathbf{\Psi} - \tilde{\mathbf{\Psi}}), \tag{9}$$

where $\mathbf{H}_\Psi$ includes the second order derivative with respect to the elastic parameters:

$$(\mathbf{H_\Psi})_{ijk}(\tilde{\mathbf{\Psi}}, \mathbf{m}) = \frac{\partial^2 g_i}{\partial \Psi_k \partial \Psi_j}(\tilde{\mathbf{\Psi}}, \mathbf{m}). \tag{10}$$

From equation 9, we can then calculate the $\mathbf{C_p}$ matrix using equation 5 by rapidly generating a large number of forward model predictions.

The derivatives in equation 9 are computed numerically using finite differences. We summarize the difference in computational cost between approaches in table 1. The computational cost of each approach in terms of forward model evaluation is summarized in Table 1. In this study, the empirical approach necessitated about 200 forward model evaluations, which is much less than what is necessary when using a 2nd order approach. However, the computational cost is significantly reduced when considering 1st order derivatives or 2nd order derivatives without cross-terms. In the following, we will only consider the empirical, first order and 2nd order without cross-terms approaches.

In Figure 4 and Figure A4, we compare the diagonal of the $\mathbf{C_p}$ matrix for HRGPS and strong motion stations. The 1st and 2nd order matrices seem to capture the main features of the empirical $\mathbf{C_p}$ matrix. Overall, the diagonal elements of the 2nd order $\mathbf{C_p}$ are more similar to the empirical $\mathbf{C_p}$ matrix. Even if the 2nd order $\mathbf{C_p}$ is computed after neglecting 2nd order cross-terms in equation

Table 1. Approaches to calculate $\mathbf{C_p}$ (for 36 parameters)

Approach.	Number of forward model evaluations
Without $\mathbf{C_p}$	0
Empirical	195 (in this study)
1st order Forward Derivatives	37
1st order Centered Derivatives	72
2nd order without cross-terms	73
2nd order	1333

9, Figure A5 shows that the difference with respect to the empirical $\mathbf{C_p}$ matrix is 10-20 % smaller than the 1st order $\mathbf{C_p}$ matrix. Such differences could impact the inversion results. For this reason, in the next section, we explore the impact of the type of $\mathbf{C_p}$ matrix estimate on the coseismic models of the 2015 $M_W = 8.3$ Illapel earthquake.

To model the 2015 $M_W = 8.3$ Illapel earthquake, we design a curved fault geometry using the GOCAD® commercial software package matching local seismicity and aftershock focal mechanisms (Figure 1). The focal mechanisms are from Global CMT (Dziewonski et al. 1981) over a period of one month after the mainshock. The fault surface is divided into 10 patches along-dip and 17 patches along-strike (170 in total) with 18 km side-length, which in a sense, is a spatial regularization. However, we do not impose any smoothing or empirical regularizations in the inverse problem, which could potentially smooth out rupture complexities. For the static inversion, we invert for along-strike and along-dip slip components in each subfault. In the full joint inversion, we invert for both slip components along with rise time, rupture velocity, and the hypocenter location on the fault (along-strike and along-dip distance). We model the rupture front by solving the eikonal equation for a candidate rupture velocity in each subfault. Each subfault is discretized into 10×10 point sources that rupture sequentially as the rupture front passes. During the earthquake, each point on the fault is allowed to rupture only once (contrary to a multi-window approach such as from Hartzell & Heaton (1983) or Li et al. (2016)), adopting a prescribed triangular slip rate function. Even though multi-window approach is able to recover great complexity in the slip rate functions, the single window approach works better for recovering rupture velocity and seismic

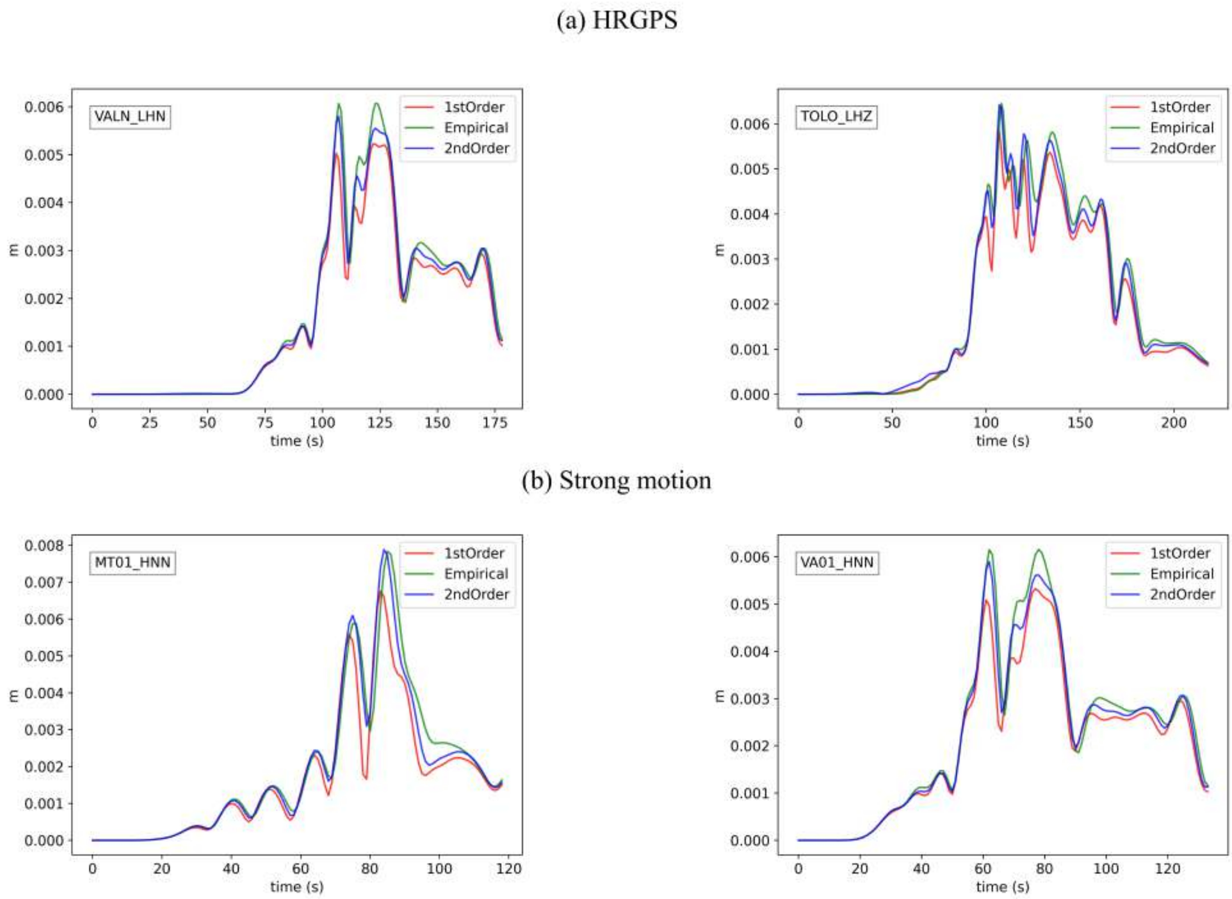

Figure 4. Covariance matrix comparison for HRGPS records (a) and Strong Motion stations (b). The green line represents the diagonal of the empirical covariance matrix (i.e., the matrix created from an ensemble of models). The red and blue line represents the diagonal of the matrix calculated using the 1st and 2nd order approximation approach.

moment and at the same time, it significantly decreases the number of inverted parameters (Cohee & Beroza 1994).

In the Bayesian inversion approach, we describe a priori PDFs to represent our prior knowledge for each of the parameters to invert. The corresponding *a priori* distributions of our joint model are shown in Figure A6. We use the hypocenter of the CSN as *a priori* since it was obtained using regional data. For InSAR images, we include a nuisance parameter to correct each image from a constant offset (i.e., two nuisance parameters in total), and for the GPS data sets we add translation parameters (i.e., three parameters for each set). These parameters are used to redefine the reference frame of each geodetic dataset during the inversion process, since both InSAR and GNSS are relative measurements, and have their own reference frame.

Since we are working with different data sets, we want to know how sensitive they are to slip on the fault. Thus, we carry out a sensitivity analysis for each data set. We follow the approach similar to Duputel et al. (2015). The sensitivity of each data set is calculated as:

$$\mathbf{S}(D) = \mathrm{diag}(\mathbf{G}^t(D) \cdot \mathbf{C}_\chi^{-\mathbf{1}}(D) \cdot \mathbf{G}(D)), \tag{11}$$

where $\mathbf{G}$ is the corresponding Green functions (in the along-dip direction), and $\mathbf{C}_\chi$ is the covariance matrix described above for a given data set D. For a given subfault, this measure is equivalent to computing the L_2 norm of the predictions due to unit dip-slip in the considered patch. The corresponding sensitivities are shown in Figure A7. GPS and InSAR data sets are sensitive to slip in most fault areas, except for the shallowest region. On the other hand, tsunami data is not sensitive to slip in the inshore fault region but to the offshore zone. The kinematic data is globally sensitive to slip over the entire fault. Finally, if we use the whole data set, although we still observe a decrease in sensitivity at the trench, we have an overall good sensitivity to slip over the entire fault.

4 RESULTS

According to our cascading approach, we first perform an inversion of the final slip using static data (that is, InSAR, GPS and tsunami data). We thus generate a posterior ensemble of slip models whose posterior mean and uncertainty is shown in Figure 5. This model presents two main slip patches that extend up-dip to the trench. The solution obtained using static data only has a peak slip of about 10.9 +/- 16.0 meters, while the mean fault slip is about 2.5 +/- 1.8 meters (assuming a 95% confidence interval). We observe that uncertainties are as large as the posterior mean slip amplitude. In addition, we see that even if tsunami data is employed, slip uncertainty is larger in the shallow part of the fault, due to the lack of data coverage in that area.

We then use the *a posteriori* PDF of the static slip model as a starting point to make three different joint inversions: i) a joint inversion using an empirical $\mathbf{C_p}$ matrix, ii) a joint inversion using a $\mathbf{C_p}$ matrix calculated using the first-order perturbation approach, and iii) a joint inversion using a $\mathbf{C_p}$ matrix calculated using the second-order perturbation approach. The posterior mean

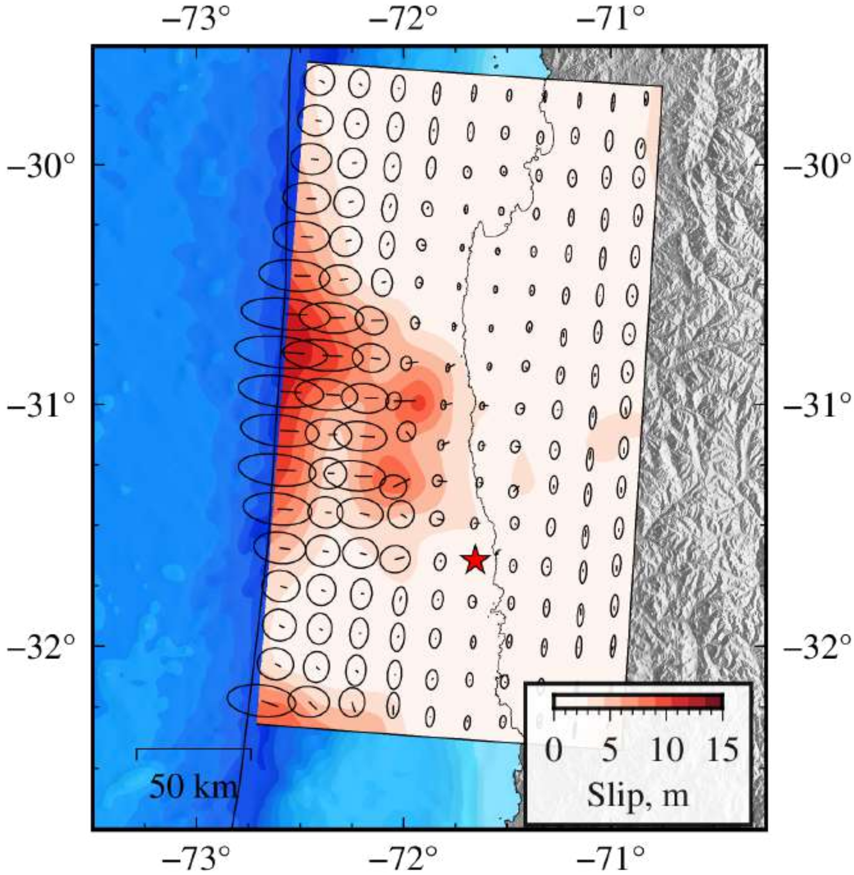

Figure 5. Posterior mean coseismic slip model for the static data set. Arrows represent the slip directions and the ellipses their associated uncertainties assuming a 95% confidence interval.

coseismic slip models obtained using these different approaches are shown in Figure 6. We also compare the posterior distributions of dip-slip in the online supplement (Figure A8). The three solutions exhibit two principal slip regions, one northwestward of the hypocenter and another at shallow depth reaching the trench. The deeper slip patch is well constrained for the three solutions, with a mean slip of 6 to meters for this region. The solution based on 1st order $\mathbf{C_p}$ shows a compact slip patch at shallow depth, while shallow slip is more broadly distributed when considering 2nd order or empirical $\mathbf{C_p}$ matrices. This results into a larger peak slip value for the 1st order $\mathbf{C_p}$ solution (21.0 +/- 4.1 meters), while solutions obtained with an empirical $\mathbf{C_p}$ (15.88 +/- 5.0 meters) and with a 2nd order $\mathbf{C_p}$ (17.63 +/- 6.8 meters) display smaller peak slip values. Uncertainties significantly decrease when incorporating the kinematic data set.

Figure 7 compares rupture times between solutions (taking the solution based on empirical $\mathbf{C_p}$ as reference). Both models obtained using a first and second order $\mathbf{C_p}$ result in rupture times

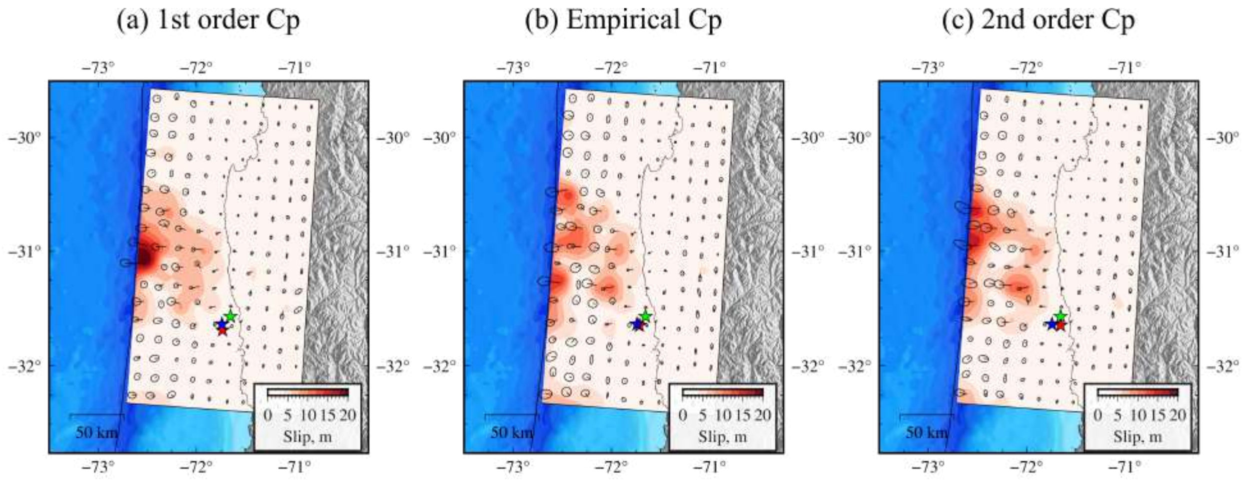

Figure 6. Comparison of co-seismic slip distributions obtained using different prediction error covariances $\mathbf{C_p}$. Red colors indicate the corresponding posterior mean coseismic slip model . Arrows represent the slip directions with their corresponding uncertainty shown by ellipses. The red star is the inverted hypocenter location (empirical, 1st, and 2nd order approximation, respectively). The blue star is the CSN hypocenter, and the green star is the USGS hypocenter.

similar to those obtained with an empirical covariance matrix. However, the second order approach presents an overall smaller dispersion ($\sigma = 4.75$ seconds) compared to the first order approach ($\sigma = 5.97$ seconds). Regardless of the prediction error covariance matrix, we note that the nuisance parameters associated with GPS data sets converge to zero, which means they don't need further corrections (Figure A9). There is no significant variation in the constant offset associated with the descending InSAR image, with a posterior mean value of 3.7 cm. On the other hand, there are some differences in the nuisance parameter of the ascending interferogram, which vary between -2.5 cm and -1.5 cm between the different solutions.

Details of the solution obtained using a 2nd order $\mathbf{C_p}$ are shown in Figure 8. Similar figures are presented for the 1st order and empirical $\mathbf{C_p}$ in supplementary Figures A10 and A11, respectively. Stochastic rupture propagation fronts in Figure 8 (a) suggest a complex rupture pattern. It slowly grows close to the hypocenter, and then propagates updip, with a rupture speed from 2 to 4 km/s. Stochastic moment rate functions in Figure 8 (b) indicate an overall rupture duration of 120 seconds approximately. The average scalar seismic moment is $M_0 = 3.20 \pm 0.045 \times 10^{21}\mathrm{N \cdot m}$, i.e., a moment magnitude of $M_W = 8.27 \pm 0.005$. We can notice two energy peaks, a small one at 25 seconds, and another one at 50 seconds. As it has been reported before (Gombert et al. 2018b), we

(a) 1st order Cp (b) 2nd order Cp

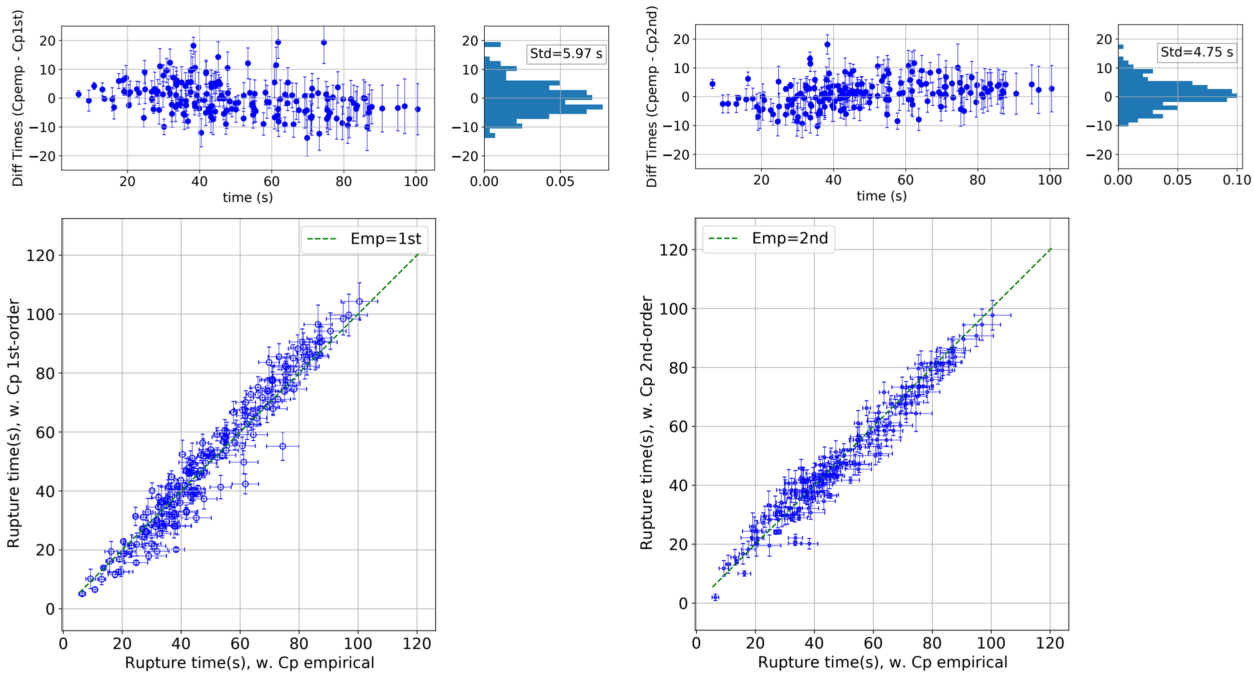

Figure 7. Rupture times comparison between different $\mathbf{C_p}$ inversion solutions. Comparison between the empirical covariance matrix and the first order (a) and 2nd order (b) approaches.

observe a negative correlation of rise time and initial rupture times (Figure A12 (a)). However, this correlation disappears when comparing rise time and slip pulse centroid times (Figure A12 (b)). This arises from the fact that observations are more sensitive to the slip pulse centroid time at each subfault, rather than the initial rupture time and rise time (see Fig. 7; Gombert et al. 2018b). The distribution of centroid times in Figure 8 (c) shows a heterogenous rupture propagation. In particular, there are regions at the northwest of the hypocenter that break faster than their corresponding adjacent areas. These complexities are discussed further in section 5.2.

We use the posterior coseismic model to calculate synthetic displacements and compare them to GPS observations (Figure 9). Both permanent stations and campaign survey stations show an acceptable fit, including the vertical components. The corresponding residuals are shown in Figure A13. The residuals are globally small compared with uncertainties. For the horizontal components, the average residual is approximately 10 centimeters, while for the vertical component is 5 centimeters, which is acceptable given the magnitude of the displacements (up to 2 meters). Stochastic predictions of tsunami waveforms display a good agreement with tsunami observations

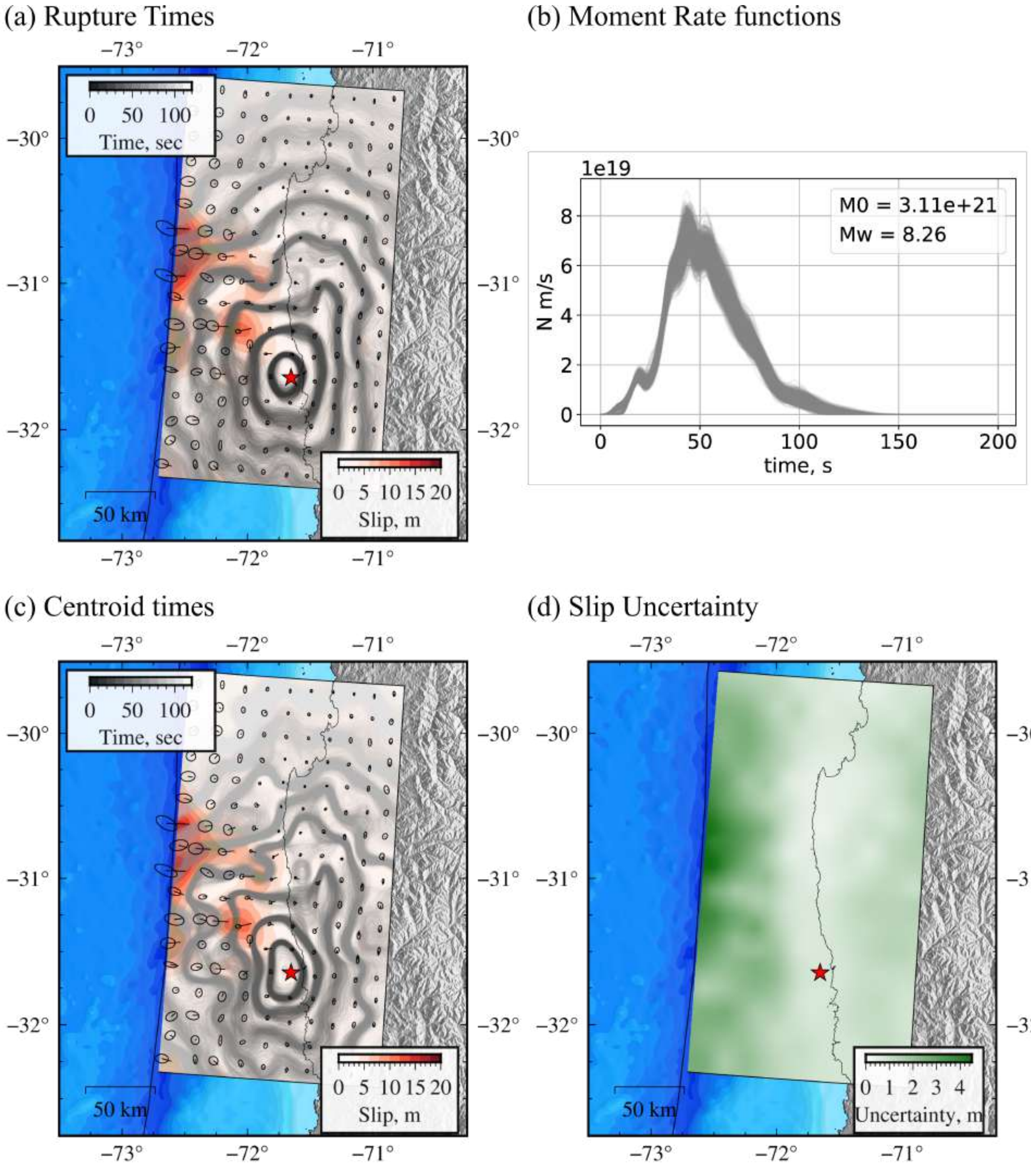

Figure 8. Impact of using a 2nd order approximation $\mathbf{C_P}$ in slip inversion. (a) Posterior mean coseismic slip model, arrows represent the slip directions and the ellipses its corresponding uncertainty. Contours show stochastic rupture fronts samples from the *a posteriori* distribution every 10 seconds. (b) Stochastic moment rate functions. (c) Posterior mean coseismic slip model with contours that represent stochastic centroid time fronts samples from the *a posteriori* distribution. (d) Uncertainty of the ensemble of coseismic slip models. The red star in the figures represents the inverted hypocenter location.

(Figure 10). In particular, we see that later arrivals are often well fitted even if they are not included in the data set used for the slip inversion. The tide gauges buca1, papo1, and talt1, and the DART stations D32411, D43412, and D51407 present a slight time-shift between observed and predicted waveforms. This shift could be explained by local site effects, local bathymetry for the case of tide gauges, and in the case of DART stations, by path trajectory not accurately modeled by the forward model. Figure 11 shows that InSAR data is also well predicted by our posterior coseismic model, with residuals smaller than 10% of maximum LOS displacements. The spatial distribution of the residuals does not correlate with the co-seismic displacement pattern. Nevertheless, we notice a spatial pattern in the InSAR residuals from Figure 11 (c), with more positive values in the northern region of the image. This residual could be linked to discrepancies between different types of geodetic observations in the region. While the ascending image shows vertical displacements up to 40 centimeters, GPS vertical displacements in the same area are close to zero or even display negative values. This InSAR residual pattern has also been observed by Klein et al. (2017). We also use the posterior coseismic model to calculate kinematic stochastic waveforms. Kinematic data show a directivity effect with larger amplitudes toward the north that is well reproduced by the model (Figures 12, and A14). We can see that stochastic waveforms reproduce most of the features visible in the HRGPS and strong motion records, even at large distances (i.e., distances$>2°$).

5 DISCUSSION

We compare our slip models with previous models published in the literature. Our posterior coseismic model presents a maximum slip of 17.63 +/- 6.8 meters at shallow depth. This slip magnitude is larger than the one observed by Klein et al. (2017) (10 meters), An & Meng (2017); Ruiz et al. (2016); Shrivastava et al. (2016) (8 meters), and previous kinematic models such as the one of Heidarzadeh et al. (2016); Li et al. (2016); Melgar et al. (2016); Tilmann et al. (2016) (6-12 meters). Overall, our joint model is more similar to the slip distribution of Melgar et al. (2016), which exhibits two slip regions, with a maximum slip of 12 meters, which is smaller than our posterior mean estimate but within uncertainty of our solution. This difference likely results from the

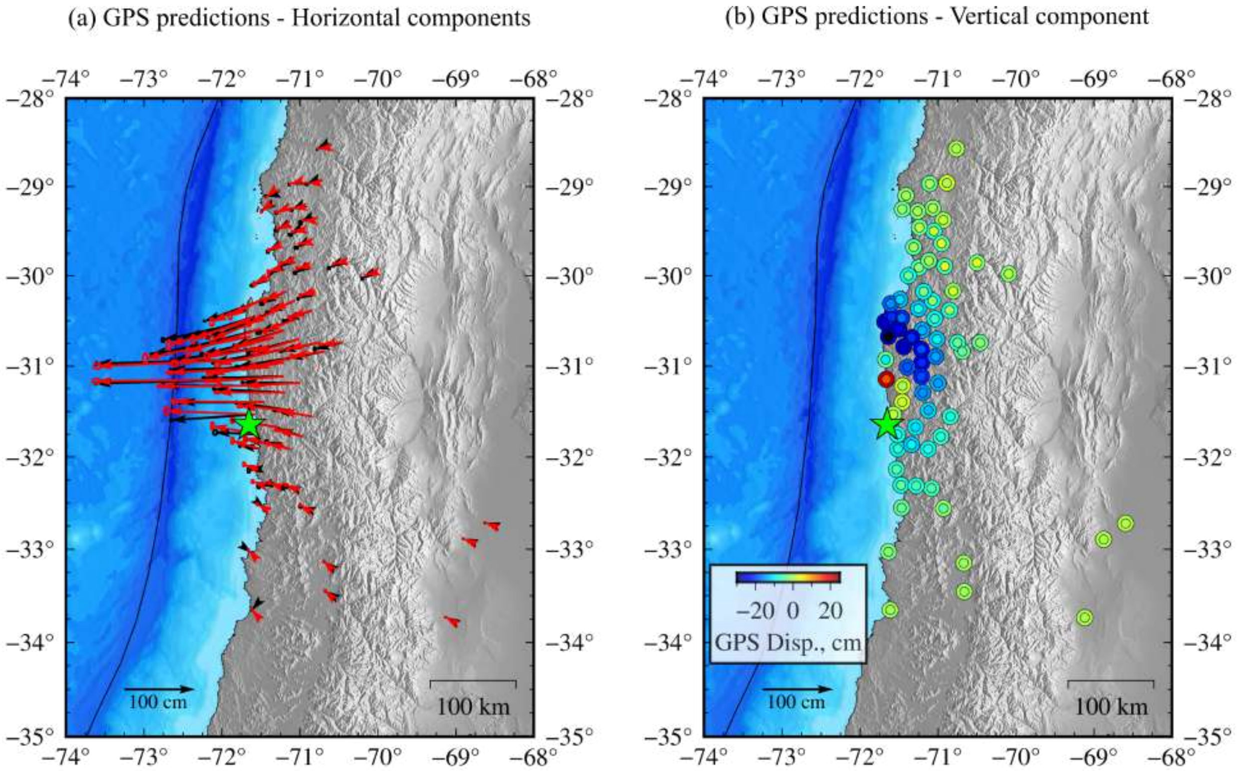

Figure 9. (a) Observed horizontal GPS (black arrows) and predictions for the posterior mean model (red arrows) using a 2nd order approximation $\mathbf{C_p}$. (b) The colormap indicates vertical component displacements for observed GPS (outer circle) and vertical predictions for the posterior mean model (inner circle).

fact that our results rely only on spatial discretization in square subfaults while the inversion does not incorporate on smoothing constraints, contrary to the aforementioned studies that incorporate smoothing regularizations. By using such constraints, the slip distributions are smoother, which penalizes abrupt changes and locally high slip amplitudes.

While largest slip amplitudes in our posterior model are located at relatively shallow depth, we note that several previously published models include slip extending to deeper regions of the fault (i.e., below the coast). In this regard, Klein et al. (2017) suggest that slip at larger depth is necessary to fit vertical GPS observations. While the fault slips mostly offshore according to our solution, we still observe significant slip (2-3m) at larger depth. In Figure A15, we investigate the contribution of slip at different depths to fit the vertical GPS observations. In agreement with our sensitivity maps in Figure A7, we see that shallow slip does not generate much displacement inland. Although we see that a moderate amount of slip close to the coast generates uplift in our model predictions, our model still features some misfits on coastal GPS stations (as shown in

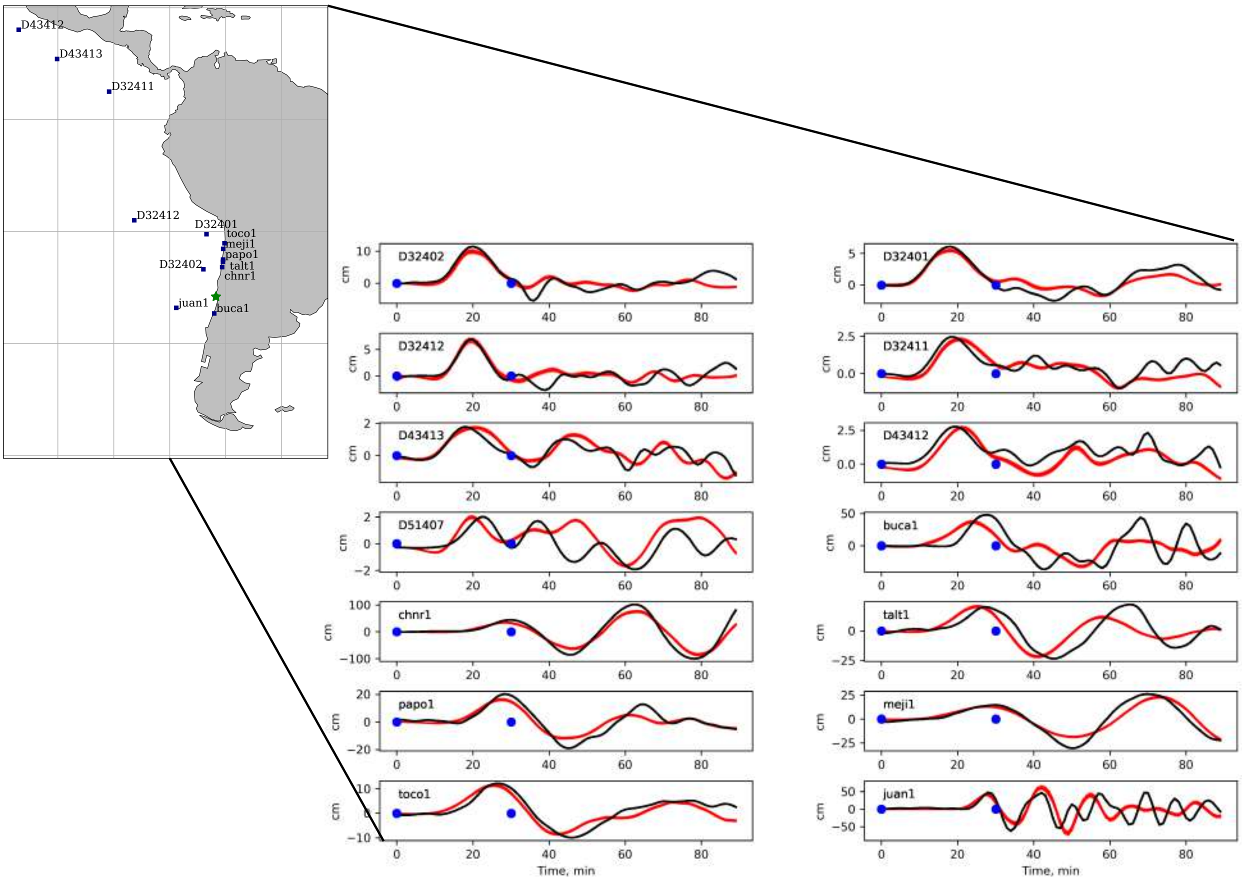

Figure 10. Comparisons between tsunami observations (black) and stochastic predictions (red) using a 2nd order approximation $\mathbf{C_p}$. The tsunami waveform signal used in the inversion is shown between blue dots. The map depicts each tsunami station locations.

Figure A13), which can explain the difference in the amount of slip at depth compared to previous models (e.g., at station EMAT with an observed uplift of 20 cm, Klein et al. (2017) has a misfit of 5 cm while our solution corresponds to a misfit of 8 cm).

In the next subsections, we will examine individually different aspects of the Illapel earthquake rupture. We first assess the reliability of our model close to the trench by exploring the importance of shallow slip to fit tsunami records. We then investigate encircling rupture patterns visible in our solutions.

5.1 Impact of Shallow slip.

At present, there is no general agreement regarding the amount of shallow slip during the Illapel earthquake since some studies indicate the absence of shallow slip (An & Meng 2017), while

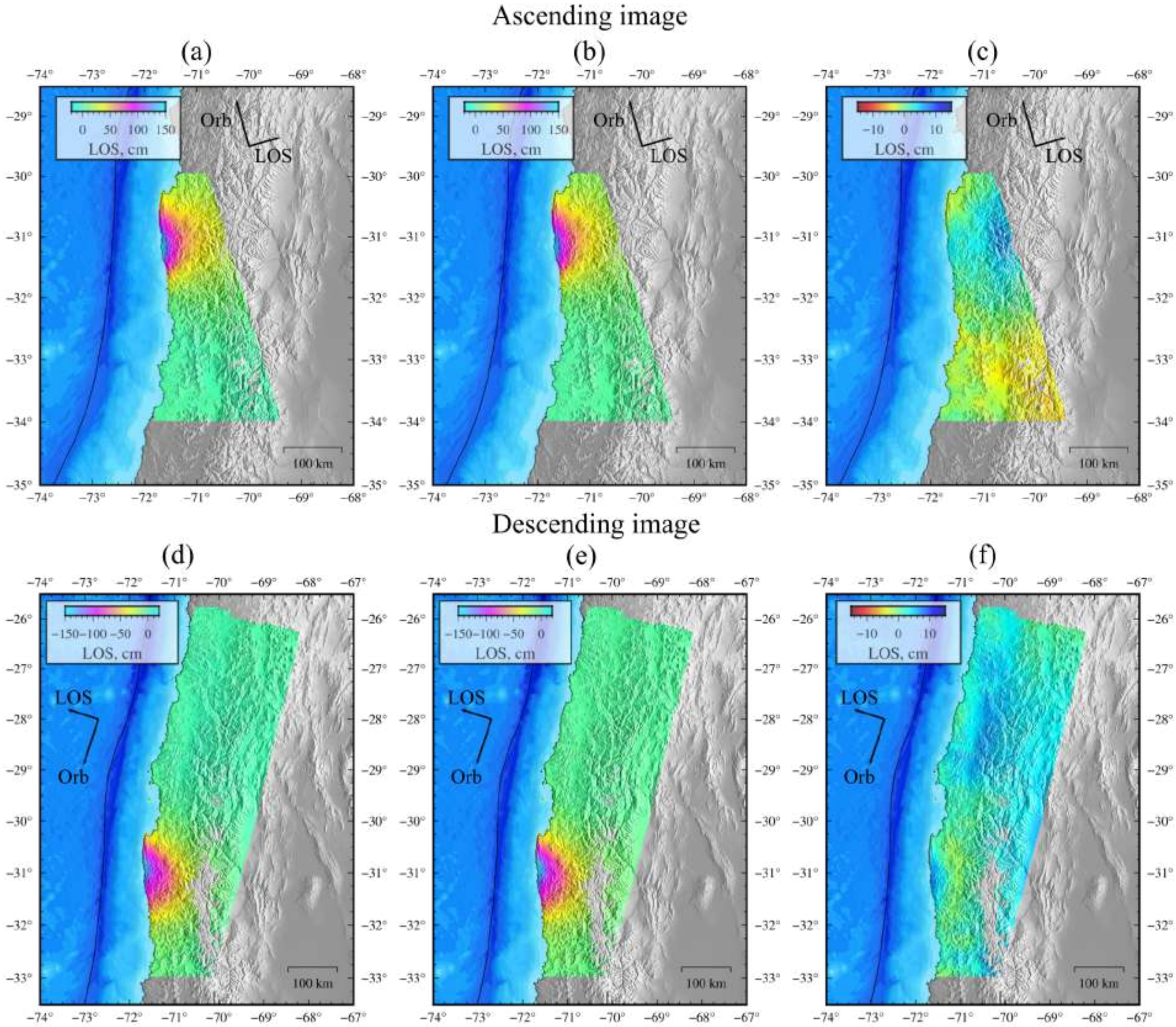

Figure 11. InSAR misfit using the posterior coseismic model using the 2nd order $\mathbf{C_p}$ matrix solution. Observed ascending (a) and descending (d) Sentinel-1A images. We show the corresponding synthetic displacement for ascending (b) and descending (c) images and the respective residual, ((c) for ascending, and (f) for descending images). Small black arrows represent the LOS and orbit direction, respectively.

others demonstrate that shallow slip is necessary to explain tsunami observations (Lay et al. 2016). To analyze the amount of shallow slip, we evaluate the cumulative posterior PDF of slip in the shallow region (Figure 13). We observe that the probability of slip to be greater than 13 meters at shallow depth is about 83.8 %.

To further explore the contribution of shallow slip, we perform a static slip inversion imposing shallow slip to be very small (i.e., in the two shallowest subfault rows). The aforementioned was performed by fixing a prior PDF with a narrow gaussian centered on zero for the along-dip com-

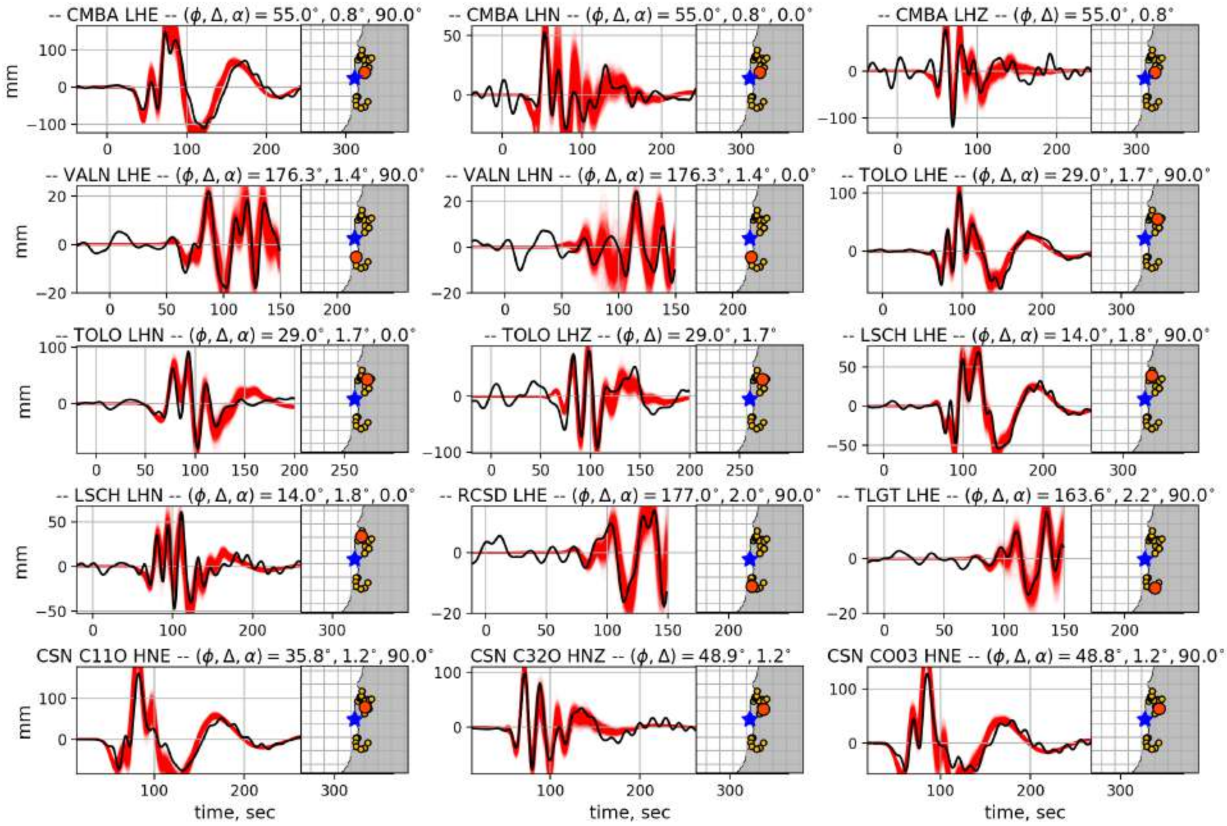

Figure 12. Examples of comparisons between data (black) and stochastic predictions (red) for HRGPS and Strong Motion stations using a 2nd order approximation $\mathbf{C_p}$. On the maps, the blue star represents the hypocenter while circles indicate station location (orange for the station depicted and yellow for the other stations). ϕ and Δ represent the azimuth and distance from the epicenter. The angle α is the horizontal component azimuth ($0°$ -north, $90°$ -east).

ponent of slip (considering a standard deviation of 0.5 meters). The corresponding posterior mean model is shown in Figure 14. If we compare the resulting solution in Figure 14 with the previous posterior coseismic models in Figure 5 and Figure 8, we can still find the slip patch close to the hypocenter (longitude $-72°$, latitude $-31.25°$). However, the shallow part of the model is significantly different due to the new prior. Regarding the data fit, we can notice that GPS fits remain unchanged between static models (Figure A16) (i.e., GPS observations are insensitive to shallow slip). The comparison of model performance for tsunami observations for both solutions is shown in Figure 14 (b). We notice that the RMS misfit for tsunami data are smaller when including shallow slip (Figure A17). However, such comparison can be misleading: the model with shallow slip will naturally better fit the observations as it includes more free parameters than the one for which shallow slip is proscribed. To evaluate if the decrease in tsunami misfit is significant, we evaluate two different information criteria: The Bayesian Information Criterion (BIC) and the Akaike Information Criterion (AIC) (Bishop 2006) (supplementary information text S5). In Table 2 we show the differences ΔBIC and ΔAIC, with respect to our solution including shallow slip. Both criteria tend to favor occurrence of shallow slip rather than the solution without slip at shallow depth (i.e., the model with shallow slip is associated with smaller BIC and AIC values). In other words, the difference in RMS misfit is sufficient to justify the existence of slip at shallow depth. It is worth mentioning that tsunami data is the only data set controlling the slip at shallow depth since is the most sensitivity data to this feature (as shown in the sensitivities in Figure A7. The differences with previous back-projection studies come from the fact that such shallow features are difficult to resolve only using seismic information (as pointed out by Lay et al. (2016)).

Finally, we compare the posterior mean joint coseismic slip distribution with aftershocks locations (Figure 15). We observe aftershocks in the outer-trench zone, distributed along the shallow slip region revealed by our solution. As suggested by Sladen & Trevisan (2018), the occurence of outer-rise aftershocks can be used as a proxy to estimate the occurence of slip at shallow depth along the subduction interface. The distribution of aftershocks is therefore consistent with the occurrence of shallow slip during the Illapel earthquake.

The existence of large slip at shallow depth supports the fact that the 2015 event is not a simple repeat of the earthquake that affected the region in 1943 (Tilmann et al. 2016). This is consistent with historical reports indicating that the tsunami generated in 1943 was much smaller than what was observed in 2015. In addition, the differences in the duration of teleseismic body-wave arrivals for both events suggest that the 1943 rupture did not involves shallow slip (Tilmann et al. 2016). The reason why the 2015 event involves shallow slip contrarily to the 1943 event is unclear. One possibility is that shallow slip deficit was larger in 2015 than in 1943. This is consistent with coupling models from Métois et al. (2016) showing that the fault is not creeping at plate rate at shallow depth. However, this remains speculative as fault coupling close to the trench

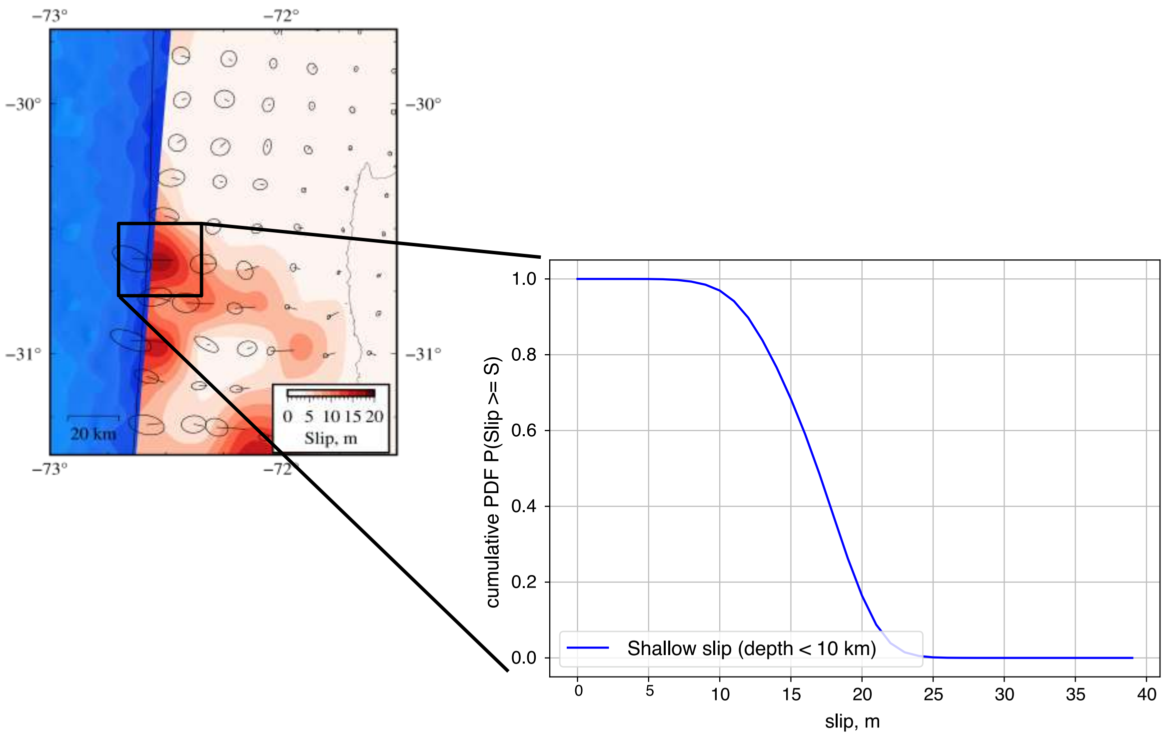

Figure 13. Cumulative probability of having a slip greater or equal to a corresponding amplitude for a subfault experiencing large slip at shallow depth. The corresponding subfault is shown in the inset figure on the left. Colors represent the posterior mean coseismic slip model using the 2nd order approximation approach. Arrows and ellipses represent the slip directions and their corresponding uncertainties, respectively.

is poorly resolved by land-based geodetic data and could potentially be biased when ignoring stress shadowing effects (Lindsey et al. 2021).

Table 2. BIC and AIC values with and without shallow slip. Bayesian (BIC) and Akaike (AIC) information criteria are defined in supplementary text S5. ΔBIC and ΔAIC are the difference in BIC and AIC values with respect to the slip model including shallow slip. The values suggest that the shallow slip should be included to properly explain the observations.

Model	ΔBIC	ΔAIC
Shallow slip (348 parameters)	0	0
No shallow slip (314 parameters)	1001	1096

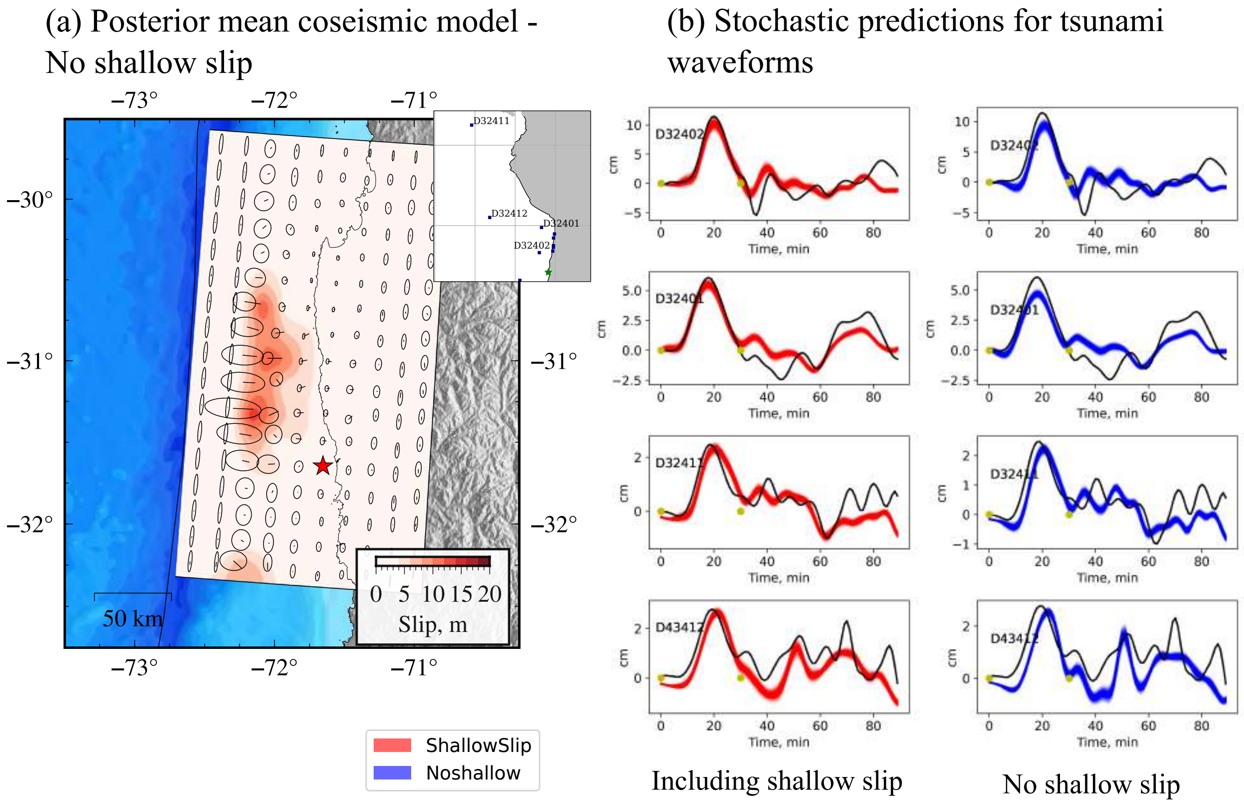

Figure 14. (a) Posterior mean coseismic slip model for a static inversion with a non shallow slip *a priori*. Arrows represent the slip directions and the ellipses their associated uncertainties. (b) Comparisons between tsunami observations (black) and stochastic predictions with shallow slip (red) and without shallow slip (blue). The tsunami waveform signal used in the inversion is shown between yellow dots. The map shows the depicted tsunami stations in (a).

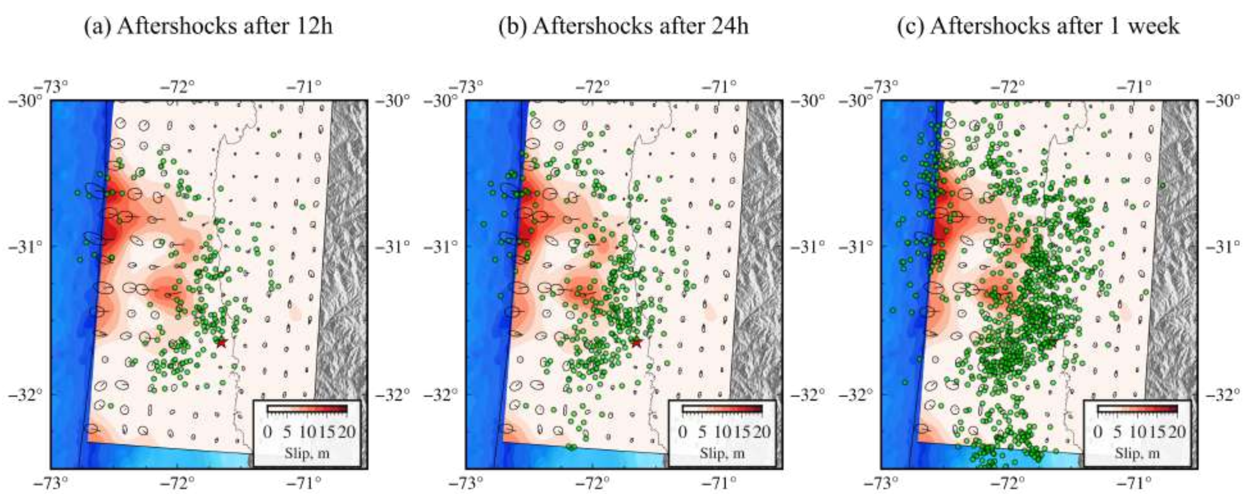

Figure 15. Comparison of posterior coseismic mean model with ISC aftershocks locations (green dots) after 12 hours (a), 24 hours (b), and one week after the mainshock (c). The red star is the inverted hypocenter location. Arrows represent the slip directions with their corresponding uncertainty shown as ellipses.

5.2 Encircling rupture pattern during the 2015 Illapel earthquake.

Back-projection results from Meng et al. (2018) show an encircling rupture during the 2015 Illapel earthquake. However, this encircling effect has not been reported by any previous kinematic slip inversion model. Results in Figures 8 (a) and (c) show a possible encircling behavior northwestward from the hypocenter location. We use the posterior coseismic mean model to investigate the slip and slip rate evolution. Snapshots from the slip rate history (supplementary movie 1) and slip history (supplementary movie 2) are shown in Figures 16 and A18, respectively. The rupture slowly grows propagating up-dip for 38 seconds. During this first stage of the rupture, we observe two different slip rate patches in supplementary movie 2, a main region in the up-dip fault area, and at 32 seconds, a secondary slip rate patch in the down-dip region. This secondary patch rapidly vanishes after a few seconds, without producing significant slip. Different back-projection studies show a down-dip high-frequency source, that radiates energy for at least 60 seconds (An et al. 2017; Melgar et al. 2016). Even though the down dip slip rate in our model is only activate for 30 seconds, the location of this patch is similar to the aforementioned back-projection sources. Our single window parameterization could explain this difference in duration as a subfault cannot break several times in our model. However, if we compare the moment rate function of the slip model proposed by An et al. (2017) for the up-dip and down-dip regions with the results of Figure 8(b), we see that we have similar moment rate functions.

Around 40 seconds after origin time, the rupture separates in three pulses depicting a first encircling pattern up-dip from the hypocenter and then another encircling pattern above the first one, also up-dip from the hypocenter (Figure 16 and Supplementary Movie 2). These encircling slip pulses contour fault areas with smaller slip rates. This is illustrated in Figure 17 showing the posterior mean peak-slip rates for every point on the fault. All rupture branches finally join together generating a large slip-rate pulse around 60 seconds, continuing toward the north along the trench until the end of the earthquake. To investigate the reliability of these encircling rupture patterns, we examine the variability of model samples drawn from the posterior PDF. This is shown in the supplementary movie 3, which shows the variability of subfault peak slip rates for different samples of our solution. We clearly see that the two encircled regions are consistently surrounded by areas of larger slip rates. This suggests that the two encircling patterns are robust features of our solution.

To identify which part of the waveform is related to the encircled region, we calculate theoretical S wave travel times before and after the first encircled region (Figure A19). Between these arrival times, we identify a very sharp positive pulse on the east components of stations, in both HRGPS and strong motion, at the north of the hypocenter. This observation is quite consistent with simulations provided by Page et al. (2005), which showed that such encircled barriers are associated with sharp secondary pulses in the seismograms. This sharp phase is less visible on southern stations, even if a longer period pulse is visible on seismograms. This difference probably results from directivity effects, which result in larger and sharper signals at the northern stations compared to the southern stations.

To analyze the behavior of slip rate functions, we examine two families of stochastic slip rate functions corresponding to different regions that present significant slip rate values at 45 and 60 seconds (shown in Figure A20). Both slip rate functions exhibit maximums that reach up to $1.0\ \mathrm{m/s}$. The slip rate functions at 45 seconds are in the middle of the fault and last around 5 seconds, while the ones at 60 seconds are at shallow depths and continue for approximately 25 seconds. Some samples of the slip rate function at shallow depth begin at the same time and even before the slip rate functions in the middle fault. Besides, the rupture seems to spend more time in the shallow slip rate patch, producing significant slip at shallow depth. The differences in the rupture and centroid time between stochastic slip rate functions can be also observed in Figure 9. Both slip rate functions suggest that the rupture follows a pulse-like behavior since the maximum slip rate duration is around 30 seconds, which is considerably shorter than the total rupture time (around 100 seconds) (Heaton 1990). Regarding the closest encircled region, we observe in Figure 9 (c) that the centroid times arrive at this region before and then at the surroundings asperities. This could be linked to the encircled region properties (e.g., the rupture velocity of the patch) but also to the effort that the rupture spends in breaking the surrounding asperities.

The encircled slip pulses visible in our solution between 30 and 60 seconds are consistent with previous back-projection results that suggest such complexities in the rupture (e.g., Meng et al.

2018; Ruiz et al. 2016). Ruiz et al. (2016) show an early stage bilateral rupture that later merged and propagated up-dip. Meng et al. (2018) report two episodes of splitting of rupture fronts, occurring both before reaching 60 seconds (an effect known as ”double encircling pincer movement” (Das & Kostrov 1983)). The first episode reported by Meng et al. (2018) is between 15 and 35 seconds, and the second, around 45 and 60 seconds. The first encircling is colocated with the static coseismic model of An & Meng (2017). Consequently, Meng et al. (2018) suggest that the encircled region is an asperity. However, this static coseismic model could miss rupture features retrieved by our joint inversion that incorporates additional static and kinematic data. As previously pointed out (Ishii et al. 2007; Tilmann et al. 2016), back-projection sources trace the progression and changes of the rupture but are not proportional to slip. Our solution is more heterogenous, presenting multiple slip areas with both encircling episodes contouring regions with small slip rates (and moderate slip), generating particularly high slip rates where the rupture focuses in the final stage of the earthquake (see time=60s, in Figure 16). In this sense, our observations suggest rather the contouring of two regions that do not slip during the rupture. Such strong changes in the rupture propagation associated with high slip rates explain the back-projection results of Meng et al. (2018). The small slip amplitude inside the contoured regions can be caused by different factors: i) these areas could correspond to coupled regions (preventing seismic slip to occur), ii) complexities at the subduction interface (e.g., due to fracture zones or seamounts) could prevent slip to propagate in these areas, or iii) the contoured regions could be far from the rupture (i.e., initial and dynamic stresses smaller than the fault strength). Regarding the coupling at the subduction interface, the model of the region proposed by Vigny et al. (2009) and updated by Métois et al. (2012) and Métois et al. (2016) shows a relatively high coupling coefficient in the Illapel earthquake area, except in the shallowest region, where the coefficient can be as low as 0.2. However, coupling close to the trench is usually poorly constrained by land-based geodetic data. The Illapel earthquake occurred in the Metropolitan segment defined by Métois et al. (2016), and is bounded in the north by the La Serena Low-Coupling Zone (LCZ). This LCZ can be related to tectonic structures, such as the Challenger Fracture Zone (CFZ) (Contreras-Reyes et al. 2015; Maksymowicz 2015). Poli et al. (2017) investigated the different fracture zones in the Illapel region (the CFZ, and the Juan

Fernández Ridge, along with secondary structures), and suggested that these structures prevented the rupture to propagate further north and south. Consistently, we observe that the northern end of our co-seismic slip zone correlates well with the CFZ. However, we don't find any correlation between fault zone structures reported by Poli et al. (2017) and the encircled areas in our model. The small slip amplitudes in the contoured regions are thus likely not caused by such structures in the subducting plate.

To further investigate these encircled areas, we compare their locations with aftershocks distribution shown in Figure 15. During the first 12 hours, we don't observe any aftershocks overlying the encircled regions. For the southern region, aftershocks depict a half semi-circle pattern that correlates well with our results. One week after the mainshock, we notice that both encircled regions remain with no significant aftershock activity. This is also shown in the two cross sections of Figure A21, showing the absence of aftershocks in the encircled regions (shown as circles in Figure A21). Several studies have linked aftershock occurrence with afterslip expansion over time (Kato 2007; Lengliné et al. 2012; Perfettini et al. 2018), often surrounding moderate/large coseismic slip areas (Mendoza & Hartzell 1988). Some fault areas around the Illapel rupture follow this behavior, with an increase in the aftershocks rate, probably accompanying post-seismic slip in regions surrounding high coseismic slip (cf., downdip slip region in Figure 15 (a)). However, the encircled areas remain seismically inactive after the mainshock. The absence of aftershocks thus suggests that afterslip does not penetrate through these regions. Furthermore, from the results of Frank et al. (2017), we observe that these two regions don't present any significant activity nine months before, and one year after the mainshock. This suggests that the region would constitute a high-strength zone (i.e., with a high yield stress) compared with its surroundings (which could potentially break in the future), a region with a low slip deficit that broke recently (i.e., low initial stress), or with a larger fracture energy (Gallovič et al. 2020). The presence of high strength barriers has been observed for other megathrust earthquakes such as the 2001 $M_W = 8.1$ Peru earthquake (Robinson et al. 2006), which was also associated with a low aftershock seismicity rate in the barrier region. On the other hand, if we consider the 1943 earthquake that occurred in the same region, and consider a fully coupled fault with a convergence rate of 67 mm/yr, the slip deficit would be

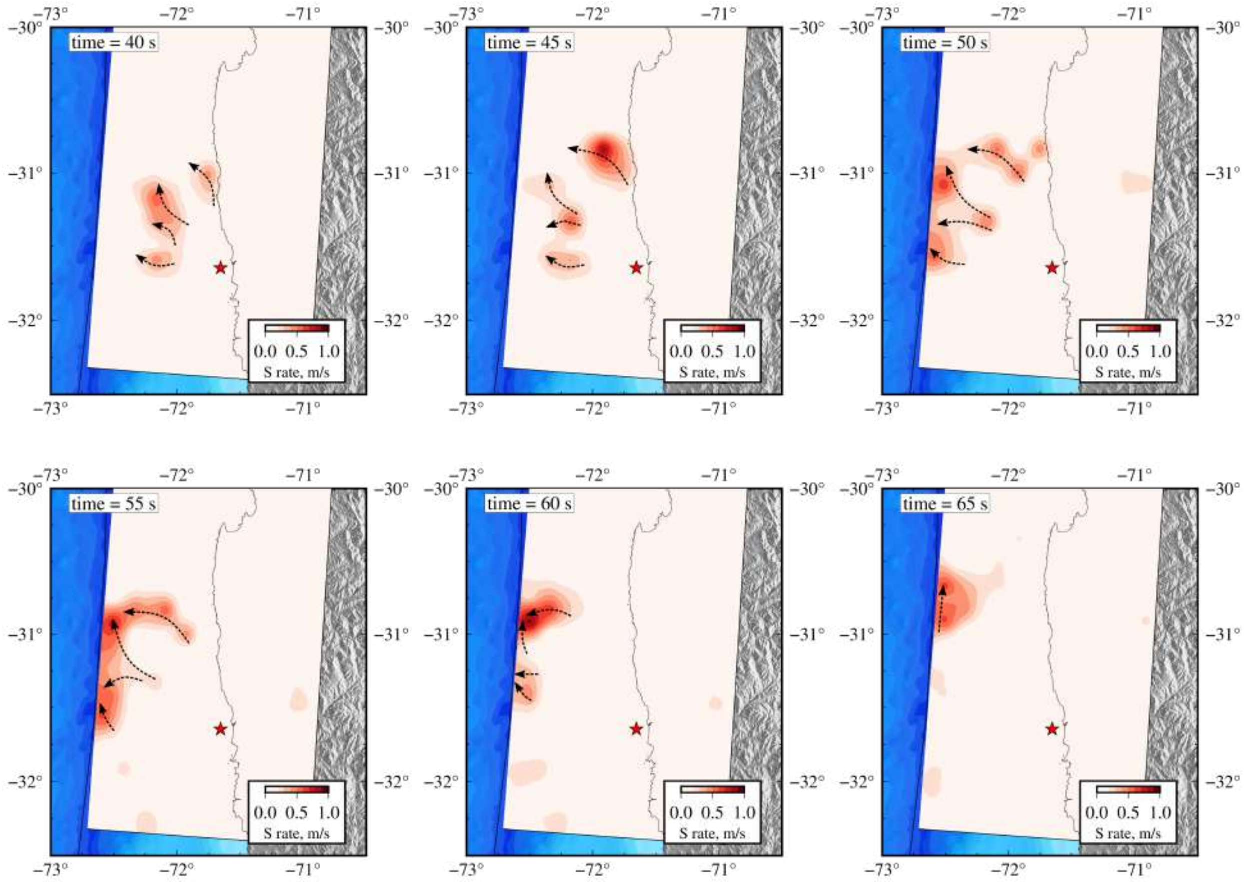

Figure 16. Five seconds snapshots of slip rate evolution. Slip rate is calculated using the posterior mean coseismic model considering the 2nd order $\mathbf{C_p}$ solution. The red star is the inverted hypocenter location. Arrow lines represent the possible encircling locations.

4.9 meters, which is small compared to adjacent areas that experienced slip up to 20 meters (cf., Figure 6). If we take this slip deficit and calculate the corresponding scalar moment, we obtain a $M_0 = 4.98 \times 10^{19}\mathrm{N} \cdot \mathrm{m}$ ($M_W = 7.06$) if they break individually, and $M_0 = 4.48 \times 10^{20}\mathrm{N} \cdot \mathrm{m}$ ($M_W = 7.7$) if they break together.

6 CONCLUSION

Using extensive geodetic, seismic and tsunami data sets, and a realistic uncertainty model, we obtain fully Bayesian finite-fault solutions of the 2015 $M_W = 8.3$ Illapel earthquake. We employ a fixed subfault geometry and a non-linear parameterization (inverting for slip, rupture velocity, rise time and hypocenter location), which allows us to resolve the complexity of the rupture. We

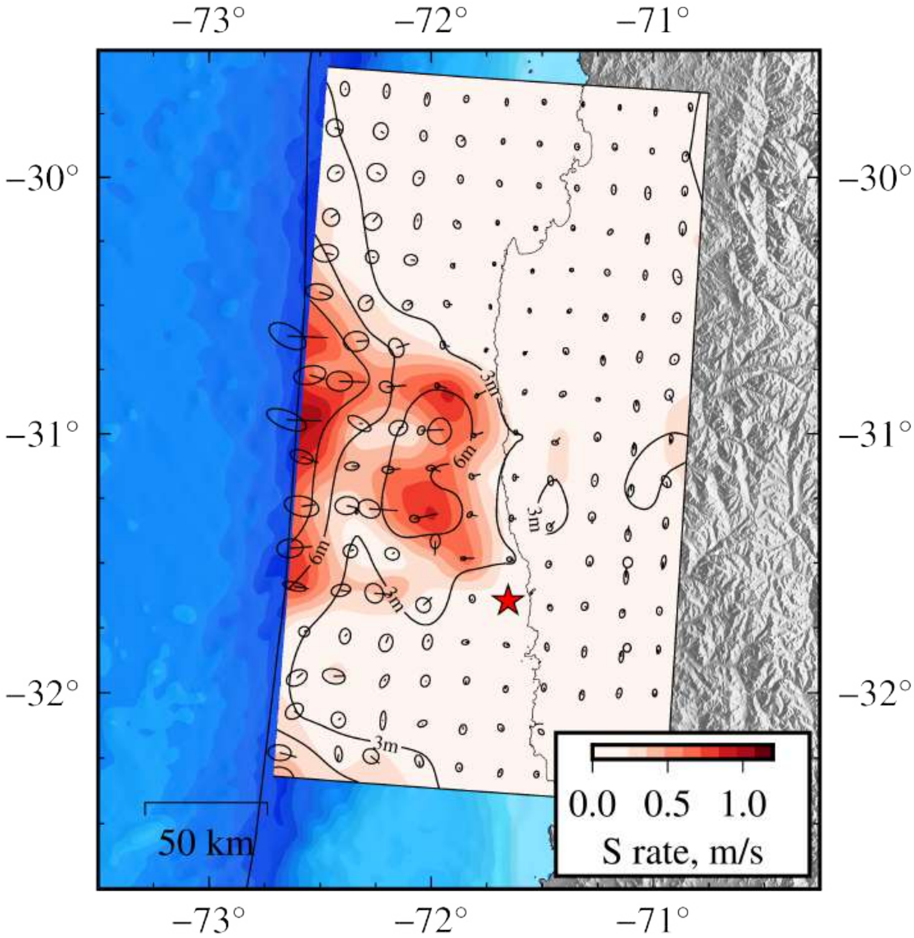

Figure 17. Posterior mean peak-slip rates. Slip rate is calculated using the posterior mean coseismic model using the 2nd order $\mathbf{C_p}$ solution. Arrows represent the slip directions with their corresponding uncertainty. The red star is the inverted hypocenter location. Black contours show the posterior mean static slip model.

also propose a 2nd order perturbation approach to better account for prediction uncertainty in seismic waveforms.

Our kinematic slip models indicate two main slip asperities : a first asperity close to the hypocenter and another one at a shallow depth. Our analysis shows that shallow slip is required to fit tsunami observations and is consistent with the distribution of outer-rise aftershock seismicity. Historical records suggest that such shallow slip did not occur during the 1943 earthquake that affected the same region of the Chilean megathrust.

Our results also highlight encircling behaviors that occur when the rupture propagates toward the trench. Such rupture complexities have been previously suggested by back-projection studies. We suggest that these encircled regions are linked to areas associated with initial and dynamic stresses smaller than the fault yield stress. Further investigations are necessary to understand whether these areas correspond to low slip deficit regions or to fault areas with high strength that could be hosting future large earthquakes.

ACKNOWLEDGMENTS

We thank H. Aochi and H. Bhat for helpful discussion. This project has received funding from the European Research Council (ERC, under the European Union's Horizon 2020 research and innovation programme under grant agreement No. 805256 and grant agreement No. 758210) and from Agence Nationale de la Recherche (project ANR-17-ERC3-0010). This research was also supported by the Mexican National Council for Science and Technology (CONACYT), scholarship 2018-000003-01EXTF-00012. RJ acknowledges funding from the Institut Universitaire de France. C. Liang was supported by National Natural Science Foundation of China under grant 42274026. A portion of this work was conducted by the Jet Propulsion Laboratory, California Institute of Technology, under contract with the National Aeronautics and Space Administration. This work contains modified Copernicus data from the Sentinel-1A satellite processed by the ESA. We thank an anonymous reviewer, Frantisek Gallovič, and Editor Eiichi Fukuyama for their valuable comments which improved this manuscript.

DATA AVAILABILITY

The seismological data used in this study were acquired by CSN Universidad de Chile (2012) and is freely accessible at the URL `http://evtdb.csn.uchile.cl/`. GPS displacements are available in Klein et al. (2017). Tide gauges are locally operated by Servicio Hidrográfico y Oceanográfico de la Armada and can be accessed at the URL `http://www.ioc-sealevelmonitoring.org`. The National Oceanic and Atmospheric Administration (NOAA) manages the DART stations accessible at `https://www.ngdc.noaa.gov/hazard/DARTData.shtml`. InSAR images were acquired by the Sentinel-1A satellite operated by the European Space Agency under the Copernicus program and raw data can be consulted at `https://winsar.unavco.org/data/access`.

REFERENCES

An, C. & Meng, L., 2017. Time reversal imaging of the 2015 illapel tsunami source, *Geophysical Research Letters*, **44**(4), 1732–1739.

An, C., Yue, H., Sun, J., Meng, L., & Báez, J. C., 2017. The 2015 mw 8.3 illapel, chile, earthquake: Direction-reversed along-dip rupture with localized water reverberationthe 2015 mw 8.3 illapel, chile, earthquake, *Bulletin of the Seismological Society of America*, **107**(5), 2416–2426.

Angermann, D., Klotz, J., & Reigber, C., 1999. Space-geodetic estimation of the nazca-south america euler vector, *Earth and Planetary Science Letters*, **171**(3), 329–334.

Beck, S., Barrientos, S., Kausel, E., & Reyes, M., 1998. Source characteristics of historic earthquakes along the central chile subduction askew et alzone, *Journal of South American Earth Sciences*, **11**(2), 115–129.

Beresnev, I. A., 2003. Uncertainties in finite-fault slip inversions: to what extent to believe?(a critical review), *Bulletin of the Seismological Society of America*, **93**(6), 2445–2458.

Bishop, C. M., 2006. *Pattern recognition and machine learning*, springer.

Bletery, Q., Sladen, A., Jiang, J., & Simons, M., 2016. A bayesian source model for the 2004 great sumatra-andaman earthquake, *Journal of Geophysical Research: Solid Earth*, **121**(7), 5116–5135.

Chen, C. W. & Zebker, H. A., 2002. Phase unwrapping for large sar interferograms: Statistical segmentation and generalized network models, *IEEE Transactions on Geoscience and Remote Sensing*, **40**(8), 1709–1719.

Cohee, B. P. & Beroza, G. C., 1994. A comparison of two methods for earthquake source inversion using strong motion seismograms.

Contreras-Reyes, E., Ruiz, J. A., Becerra, J., Kopp, H., Reichert, C., Maksymowicz, A., & Arriagada, C., 2015. Structure and tectonics of the central chilean margin (31°–33° s): Implications for subduction erosion and shallow crustal seismicity, *Geophysical Journal International*, **203**(2), 776–791.

Das, S. & Kostrov, B., 1983. Breaking of a single asperity: rupture process and seismic radiation, *Journal of Geophysical Research: Solid Earth*, **88**(B5), 4277–4288.

Duputel, Z., Rivera, L., Fukahata, Y., & Kanamori, H., 2012. Uncertainty estimations for seismic source inversions, *Geophysical Journal International*, **190**(2), 1243–1256.

Duputel, Z., Agram, P. S., Simons, M., Minson, S. E., & Beck, J. L., 2014. Accounting for prediction uncertainty when inferring subsurface fault slip, *Geophysical Journal International*, **197**(1), 464–482.

Duputel, Z., Jiang, J., Jolivet, R., Simons, M., Rivera, L., Ampuero, J.-P., Riel, B., Owen, S. E., Moore, A. W., & Samsonov, S. V., 2015. The iquique earthquake sequence of april 2014: Bayesian modeling accounting for prediction uncertainty, *Geophysical Research Letters*, **42**(19), 7949–7957.

Dziewonski, A. M., Chou, T.-A., & Woodhouse, J. H., 1981. Determination of earthquake source parameters from waveform data for studies of global and regional seismicity, *Journal of Geophysical Research:*

Solid Earth, **86**(B4), 2825–2852.

Ekström, G., Nettles, M., & Dziewoński, A., 2012. The global cmt project 2004–2010: Centroid-moment tensors for 13,017 earthquakes, *Physics of the Earth and Planetary Interiors*, **200**, 1–9.

Farr, T. G., Rosen, P. A., Caro, E., Crippen, R., Duren, R., Hensley, S., Kobrick, M., Paller, M., Rodriguez, E., Roth, L., et al., 2007. The shuttle radar topography mission, *Reviews of geophysics*, **45**(2).

Fernández, J., Pastén, C., Ruiz, S., & Leyton, F., 2019. Damage assessment of the 2015 mw 8.3 illapel earthquake in the north-central chile, *Natural Hazards*, **96**(1), 269–283.

Frank, W. B., Poli, P., & Perfettini, H., 2017. Mapping the rheology of the central chile subduction zone with aftershocks, *Geophysical Research Letters*, **44**(11), 5374–5382.

Gallovič, F., Zahradník, J., Plicka, V., Sokos, E., Evangelidis, C., Fountoulakis, I., & Turhan, F., 2020. Complex rupture dynamics on an immature fault during the 2020 mw 6.8 elazığ earthquake, turkey, *Communications Earth & Environment*, **1**(1), 40.

Geist, E. L. & Dmowska, R., 1999. Local tsunamis and distributed slip at the source, in *Seismogenic and tsunamigenic processes in shallow subduction zones*, pp. 485–512, Springer.

Gombert, B., Duputel, Z., Jolivet, R., Doubre, C., Rivera, L., & Simons, M., 2018a. Revisiting the 1992 landers earthquake: a bayesian exploration of co-seismic slip and off-fault damage, *Geophysical Journal International*, **212**(2), 839–852.

Gombert, B., Duputel, Z., Jolivet, R., Simons, M., Jiang, J., Liang, C., Fielding, E. J., & Rivera, L., 2018b. Strain budget of the ecuador–colombia subduction zone: A stochastic view, *Earth and Planetary Science Letters*, **498**, 288–299.

Hallo, M. & Gallovič, F., 2016. Fast and cheap approximation of green function uncertainty for waveform-based earthquake source inversions, *Geophysical Journal International*, **207**(2), 1012–1029.

Hartzell, S. H. & Heaton, T. H., 1983. Inversion of strong ground motion and teleseismic waveform data for the fault rupture history of the 1979 imperial valley, california, earthquake, *Bulletin of the Seismological Society of America*, **73**(6A), 1553–1583.

Heaton, T. H., 1990. Evidence for and implications of self-healing pulses of slip in earthquake rupture, *Physics of the Earth and Planetary Interiors*, **64**(1), 1–20.

Heidarzadeh, M., Murotani, S., Satake, K., Ishibe, T., & Gusman, A. R., 2016. Source model of the 16 september 2015 illapel, chile, mw 8.4 earthquake based on teleseismic and tsunami data, *Geophysical Research Letters*, **43**(2), 643–650.

Herrmann, R. B., 2013. Computer programs in seismology: An evolving tool for instruction and research, *Seismological Research Letters*, **84**(6), 1081–1088.

Hughes, I. & Hase, T., 2010. *Measurements and their uncertainties: a practical guide to modern error analysis*, OUP Oxford.

Ide, S., 2015. 4.09-slip inversion, *Treatise on geophysics, 2nd edn. Elsevier, Oxford*, pp. 215–241.

Ishii, M., Shearer, P. M., Houston, H., & Vidale, J. E., 2007. Teleseismic p wave imaging of the 26 december 2004 sumatra-andaman and 28 march 2005 sumatra earthquake ruptures using the hi-net array, *Journal of Geophysical Research: Solid Earth*, **112**(B11).

Jiang, J. & Simons, M., 2016. Probabilistic imaging of tsunamigenic seafloor deformation during the 2011 tohoku-oki earthquake, *Journal of Geophysical Research: Solid Earth*, **121**(12), 9050–9076.

Jolivet, R., Lasserre, C., Doin, M.-P., Guillaso, S., Peltzer, G., Dailu, R., Sun, J., Shen, Z.-K., & Xu, X., 2012. Shallow creep on the haiyuan fault (gansu, china) revealed by sar interferometry, *Journal of Geophysical Research: Solid Earth*, **117**(B6).

Jolivet, R., Simons, M., Agram, P., Duputel, Z., & Shen, Z.-K., 2015. Aseismic slip and seismogenic coupling along the central san andreas fault, *Geophysical Research Letters*, **42**(2), 297–306.

Jolivet, R., Simons, M., Duputel, Z., Olive, J.-A., Bhat, H., & Bletery, Q., 2020. Interseismic loading of subduction megathrust drives long-term uplift in northern chile, *Geophysical Research Letters*, **47**(8), e2019GL085377.

Jolivet, R., Jara, J., Dalaison, M., Rouet-Leduc, B., Özdemir, A., Dogan, U., Çakir, Z., & Ergintav, S., 2023. Daily to centennial behavior of aseismic slip along the central section of the north anatolian fault, *Journal of Geophysical Research: Solid Earth*, **128**(7), e2022JB026018.

Kajiura, K., 1981. 20. tsunami energy in relation to parameters of the earthquake fault model., *Bulletin of the Earthquake Research Institute*, **56**.

Kato, N., 2007. Expansion of aftershock areas caused by propagating post-seismic sliding, *Geophysical Journal International*, **168**(2), 797–808.

Klein, E., Vigny, C., Fleitout, L., Grandin, R., Jolivet, R., Rivera, E., & Métois, M., 2017. A comprehensive analysis of the illapel 2015 mw8. 3 earthquake from gps and insar data, *Earth and Planetary Science Letters*, **469**, 123–134.

Lay, T., Li, L., & Cheung, K. F., 2016. Modeling tsunami observations to evaluate a proposed late tsunami earthquake stage for the 16 september 2015 illapel, chile, mw 8.3 earthquake, *Geophysical Research Letters*, **43**(15), 7902–7912.

Lee, S.-J., Yeh, T.-Y., Lin, T.-C., Lin, Y.-Y., Song, T.-R. A., & Huang, B.-S., 2016. Two-stage composite megathrust rupture of the 2015 mw8. 4 illapel, chile, earthquake identified by spectral-element inversion of teleseismic waves, *Geophysical Research Letters*, **43**(10), 4979–4985.

Lengliné, O., Enescu, B., Peng, Z., & Shiomi, K., 2012. Decay and expansion of the early aftershock activity following the 2011, mw9. 0 tohoku earthquake, *Geophysical Research Letters*, **39**(18).

Li, L., Lay, T., Cheung, K. F., & Ye, L., 2016. Joint modeling of teleseismic and tsunami wave observations to constrain the 16 september 2015 illapel, chile, mw 8.3 earthquake rupture process, *Geophysical Research Letters*, **43**(9), 4303–4312.

Lindsey, E. O., Mallick, R., Hubbard, J. A., Bradley, K. E., Almeida, R. V., Moore, J. D., Bürgmann, R., &

Hill, E. M., 2021. Slip rate deficit and earthquake potential on shallow megathrusts, *Nature Geoscience*, **14**(5), 321–326.

Liu, P. L.-F., Cho, Y.-S., Yoon, S., & Seo, S., 1995. Numerical simulations of the 1960 chilean tsunami propagation and inundation at hilo, hawaii, in *Tsunami: Progress in prediction, disaster prevention and warning*, pp. 99–115, Springer.

Lohman, R. B. & Simons, M., 2005. Some thoughts on the use of insar data to constrain models of surface deformation: Noise structure and data downsampling, *Geochemistry, Geophysics, Geosystems*, **6**(1).

Lomnitz, C., 2004. Major earthquakes of chile: a historical survey, 1535-1960, *Seismological Research Letters*, **75**(3), 368–378.

Maksymowicz, A., 2015. The geometry of the chilean continental wedge: Tectonic segmentation of subduction processes off chile, *Tectonophysics*, **659**, 183–196.

Melgar, D., Fan, W., Riquelme, S., Geng, J., Liang, C., Fuentes, M., Vargas, G., Allen, R. M., Shearer, P. M., & Fielding, E. J., 2016. Slip segmentation and slow rupture to the trench during the 2015, mw8. 3 illapel, chile earthquake, *Geophysical Research Letters*, **43**(3), 961–966.

Mendoza, C. & Hartzell, S. H., 1988. Aftershock patterns and main shock faulting, *Bulletin of the Seismological Society of America*, **78**(4), 1438–1449.

Meng, L., Bao, H., Huang, H., Zhang, A., Bloore, A., & Liu, Z., 2018. Double pincer movement: Encircling rupture splitting during the 2015 mw 8.3 illapel earthquake, *Earth and Planetary Science Letters*, **495**, 164–173.

Métois, M., Socquet, A., & Vigny, C., 2012. Interseismic coupling, segmentation and mechanical behavior of the central chile subduction zone, *Journal of Geophysical Research: Solid Earth*, **117**(B3).

Métois, M., Vigny, C., & Socquet, A., 2016. Interseismic coupling, megathrust earthquakes and seismic swarms along the chilean subduction zone (38–18 s), *Pure and Applied Geophysics*, **173**(5), 1431–1449.

Minson, S., Simons, M., & Beck, J., 2013. Bayesian inversion for finite fault earthquake source models i—theory and algorithm, *Geophysical Journal International*, **194**(3), 1701–1726.

Mungov, G., Eblé, M., & Bouchard, R., 2013. Dart® tsunameter retrospective and real-time data: A reflection on 10 years of processing in support of tsunami research and operations, *Pure and Applied Geophysics*, **170**(9), 1369–1384.

Okuwaki, R., Yagi, Y., Aránguiz, R., González, J., & González, G., 2016. Rupture process during the 2015 illapel, chile earthquake: Zigzag-along-dip rupture episodes, *Pure and Applied Geophysics*, **173**(4), 1011–1020.

Page, M. T., Dunham, E. M., & Carlson, J., 2005. Distinguishing barriers and asperities in near-source ground motion, *Journal of Geophysical Research: Solid Earth*, **110**(B11).

Perfettini, H., Frank, W., Marsan, D., & Bouchon, M., 2018. A model of aftershock migration driven by afterslip, *Geophysical Research Letters*, **45**(5), 2283–2293.

Poli, P., Maksymowicz, A., & Ruiz, S., 2017. The mw 8.3 illapel earthquake (chile): Preseismic and postseismic activity associated with hydrated slab structures, *Geology*, **45**(3), 247–250.

Ragon, T., Sladen, A., & Simons, M., 2018. Accounting for uncertain fault geometry in earthquake source inversions–i: theory and simplified application, *Geophysical Journal International*, **214**(2), 1174–1190.

Razafindrakoto, H. N. & Mai, P. M., 2014. Uncertainty in earthquake source imaging due to variations in source time function and earth structure, *Bulletin of the Seismological Society of America*, **104**(2), 855–874.

Robinson, D., Das, S., & Watts, A., 2006. Earthquake rupture stalled by a subducting fracture zone, *Science*, **312**(5777), 1203–1205.

Rosen, P. A., Gurrola, E., Sacco, G. F., & Zebker, H., 2012. The insar scientific computing environment, in *EUSAR 2012; 9th European conference on synthetic aperture radar*, pp. 730–733, VDE.

Ruiz, S. & Madariaga, R., 2018. Historical and recent large megathrust earthquakes in chile, *Tectonophysics*, **733**, 37–56.

Ruiz, S., Klein, E., del Campo, F., Rivera, E., Poli, P., Metois, M., Christophe, V., Baez, J. C., Vargas, G., Leyton, F., et al., 2016. The seismic sequence of the 16 september 2015 m w 8.3 illapel, chile, earthquake, *Seismological Research Letters*, **87**(4), 789–799.

Satake, K. & Heidarzadeh, M., 2017. A review of source models of the 2015 illapel, chile earthquake and insights from tsunami data, *Pure and Applied Geophysics*, **174**(1), 1–9.

Shrivastava, M. N., González, G., Moreno, M., Chlieh, M., Salazar, P., Reddy, C., Báez, J. C., Yáñez, G., González, J., & de la Llera, J. C., 2016. Coseismic slip and afterslip of the 2015 mw 8.3 illapel (chile) earthquake determined from continuous gps data, *Geophysical Research Letters*, **43**(20), 10–710.

Sladen, A. & Trevisan, J., 2018. Shallow megathrust earthquake ruptures betrayed by their outer-trench aftershocks signature, *Earth and Planetary Science Letters*, **483**, 105–113.

Tilmann, F., Zhang, Y., Moreno, M., Saul, J., Eckelmann, F., Palo, M., Deng, Z., Babeyko, A., Chen, K., Baez, J., et al., 2016. The 2015 illapel earthquake, central chile: A type case for a characteristic earthquake?, *Geophysical Research Letters*, **43**(2), 574–583.

Tromp, J., Tape, C., & Liu, Q., 2005. Seismic tomography, adjoint methods, time reversal and banana-doughnut kernels, *Geophysical Journal International*, **160**(1), 195–216.

Twardzik, C., Vergnolle, M., Sladen, A., & Tsang, L. L., 2021. Very early identification of a bimodal frictional behavior during the post-seismic phase of the 2015 m w 8.3 illapel, chile, earthquake, *Solid Earth Discussions*, pp. 1–24.

Universidad de Chile, 2012. Red sismologica nacional. international federation of digital seismograph networks.

Vigny, C., Rudloff, A., Ruegg, J.-C., Madariaga, R., Campos, J., & Alvarez, M., 2009. Upper plate deformation measured by gps in the coquimbo gap, chile, *Physics of the Earth and Planetary Interiors*,

175(1-2), 86–95.

Wald, D. J. & Graves, R. W., 2001. Resolution analysis of finite fault source inversion using one-and three-dimensional green's functions: 2. combining seismic and geodetic data, *Journal of Geophysical Research: Solid Earth*, **106**(B5), 8767–8788.

Watada, S., 2013. Tsunami speed variations in density-stratified compressible global oceans, *Geophysical Research Letters*, **40**(15), 4001–4006.

Williams, C. A. & Wallace, L. M., 2015. Effects of material property variations on slip estimates for subduction interface slow-slip events, *Geophysical Research Letters*, **42**(4), 1113–1121.

Williamson, A., Newman, A., & Cummins, P., 2017. Reconstruction of coseismic slip from the 2015 illapel earthquake using combined geodetic and tsunami waveform data, *Journal of Geophysical Research: Solid Earth*, **122**(3), 2119–2130.

Yagi, Y. & Fukahata, Y., 2011. Introduction of uncertainty of green's function into waveform inversion for seismic source processes, *Geophysical Journal International*, **186**(2), 711–720.

Yin, J., Yang, H., Yao, H., & Weng, H., 2016. Coseismic radiation and stress drop during the 2015 mw 8.3 illapel, chile megathrust earthquake, *Geophysical Research Letters*, **43**(4), 1520–1528.

Zhu, L. & Rivera, L. A., 2002. A note on the dynamic and static displacements from a point source in multilayered media, *Geophysical Journal International*, **148**(3), 619–627.

APPENDIX A: SUPPLEMENTARY TEXT

Text S1. InSAR processing

InSAR images. InSAR data consist of a descending pair (20150824-20150917) and an ascending pair (20150826-20150919) acquired by the Sentinel-1A satellite operated by the European Space Agency under the Copernicus program. We used ISCE software (Rosen et al. 2012) to process the data, and Snaphu to unwrap the interferograms (Chen & Zebker 2002). We used SRTM DEM (Farr et al. 2007) to coregister the InSAR pairs, remove topographic phase and geocode the interferograms. To improve computational efficiency, we use a resolution-based resampling of InSAR observations (Lohman & Simons 2005). In the resampling process, displacement measurements are averaged over windows of sizes ranging from 0.6 to 10 km.

Text S2. Tsunami data and modeling. We use seven tide gauges (buca1, chnr1, juan1, meji1, papo1, talt1, toco1) and seven sea-bottom pressure sensor records (D32401, D32402, D32411, D32412, D43412, D43413, D51407) at NOAA DART (Deep-ocean Assessment and Reporting of

Tsunamis) stations (Mungov et al. 2013). We remove tidal signals at each station by fitting and subtracting a sinusoidal function over a time window of 25 hr before and 20 hr after the earthquake initiation time. We then lowpass-filter the data at 240 seconds, with one sample per minute. For the inversion, we only use the first 30 min time-window after tsunami arrival.

The tsunami Green's functions are computed using COMCOT (Cornell Multi-grid Coupled Tsunami Model code Liu et al. 1995) with the GEBCO (General Bathymetric Chart of the Oceans) 30-seconds bathymetry (The GEBCO_2014 Grid, version 20141103, `http://www.gebco.net`). We downsample the 30-seconds bathymetry data to a 0.4 min and 1 min grid size for near-field (D32401, D32402, D32411, and tide gauges) and far-field (other stations) simulations, respectively. We compute seafloor deformation for each slip source using a modified 1D elastic structure, where we assume that the shallowest layer of 2.6 km is ocean water. We apply a spatial filter when predicting seafloor deformation for unit slip, as a way to approximate the effect of water layer attenuation (Geist & Dmowska 1999; Kajiura 1981). To account for long-period dispersion (Watada 2013) that is not incorporated in COMCOT, each simulated tsunami waveform is corrected with a frequency-dependent shift in arrival times calculated along ray paths (near-field stations) or great-circle paths (far-field stations), following the method in Jiang & Simons (2016).

Text S3. Reduced Chi-squared statistic. The reduced χ^2_ν is a statistic indicator that allows to estimate if we correctly model a data set (Hughes & Hase 2010). We define it as:

$$\chi^2_\nu = \frac{\chi^2}{\nu} \tag{A.1}$$

ν is the degree of freedom $\nu = n - m$, where n and m are the number of observations and model parameters, respectively. χ^2 is defined as:

$$\chi^2 = \sum_i \frac{(O_i - C_i)^2}{\sigma_i^2}, \tag{A.2}$$

where O_i and C_i are observations and synthetic data, with their corresponding variance σ_i^2. In the framework of linear problems (i.e., when using GNSS data), we can use a preliminary solution to calculate the synthetic data and apply the χ^2_ν as follow:

$$\chi^2_\nu = \frac{r^{\mathrm{T}} W r}{\nu}, \tag{A.3}$$

with the residuals r, and W the weight matrix, that in our case is the inverse of the covariance matrix. We can notice that we can use χ^2_ν as a posterior correction estimate. As a general rule, $\chi^2_\nu > 1$ indicates that the corresponding variance could be underestimated or the model is not retrieving the observations. On the other hand, $\chi^2_\nu \approx 1$ means that the estimates between synthetic data and observations is in agreement with the variance.

Text S4. Observation measurement uncertainties.

The observed uncertainties are represented by the matrix $\mathbf{C_d}$. In the case of GPS data, we used the associated standard errors and incorporate them in $\mathbf{C_d}$. For the InSAR images, we use a two steps approach to calculate the corresponding $\mathbf{C_d}$. First, we compute residuals from a preliminary slip inversion, and from them, we compute an empirical covariance function as a function of the distance between observation points. Secondly, we estimate the best-fit exponential function of the covariance to build the full data covariance following Jolivet et al. (2012). Given the correlation between InSAR images pixels, the observed uncertainty matrix $\mathbf{C_d}$ is:

$$\mathbf{C_d}(i,j) = \sigma_d^2 e^{-\frac{||i,j||_2}{\lambda}}, \tag{A.4}$$

where i and j correspond to different InSAR pixels. σ_d and λ are 0.00605 m and 7.75 km, respectively.

For the kinematic data, we compute the observational uncertainty in two steps. First, we use a preliminary solution to compute synthetic waveforms and we obtain the residual between synthetic and observed data. We obtain a first order estimate of the correlation time from the autocorrelation of the residuals between observations and predictions of our preliminary solution. Then, we propose a covariance matrix similar to A.4, such as:

$$\mathbf{C_d}(t_i,t_j) = \sigma_d^2 e^{-\frac{|t_i-t_j|}{\lambda_t}}, \tag{A.5}$$

where t_i and t_j are time samples along the waveform, and λ_t is the correlation duration. For HRGPS data, the correlation duration is 10 seconds, and for strong motion data is 6 seconds. Secondly, we take as standard deviation σ_d the 20% of the maximum displacement of each waveform, and multiply the corresponding variance to the exponential correlation function (cf., A.5). Finally, we add the corresponding diagonal covariance matrix, a diagonal covariance matrix whose diagonal elements correspond to the noise level computed prior to the earthquake.

Text S5. The Bayesian Information Criterion (BIC) and the Akaike Information Criterion (AIC)

We define a data set of observations $\mathbf{d_{obs}}$, and a set of model parameters $\mathbf{m_i}$ that corresponds to a given parameterization $\mathcal{M}_i$. In our study, $\mathcal{M}_i$ corresponds either to the model with shallow slip, or the model imposing not significant slip at shallow depths.

We can write for each parameterization the corresponding likelihood function $p(\mathbf{d_{obs}}|\mathbf{m_i}, \mathcal{M}_i)$ and a prior PDF $p(\mathbf{m_i}|\mathcal{M}_i)$. Starting form the Bayes theorem, we describe the posterior distribution of parameters $\mathbf{m_i}$ for a given parameterization $\mathcal{M}_i$ and observations $\mathbf{d_{obs}}$ as:

$$p(\mathbf{m_i}|\mathbf{d_{obs}}, \mathcal{M}_\mathbf{i}) = \frac{p(\mathbf{m_i}|\mathcal{M}_\mathbf{i})\; p(\mathbf{d_{obs}}|\mathbf{m_i}, \mathcal{M}_\mathbf{i})}{p(\mathbf{d_{obs}}|\mathcal{M}_\mathbf{i})} \tag{A.6}$$

Where the denominator corresponds to the marginal likelihood, that can be written as:

$$p(\mathbf{d_{obs}}|\mathcal{M}_\mathbf{i}) = \int p(\mathbf{d_{obs}}|\mathcal{M}_\mathbf{i})\; p(\mathbf{m_i}|\mathcal{M}_i)\; d\mathbf{m_i} \tag{A.7}$$

This marginal likelihood can be used to assess the posterior distribution of different parameterizations using the available observations as:

$$p(\mathcal{M}_\mathbf{i}|\mathbf{d_{obs}}) \propto p(\mathbf{d_{obs}}|\mathcal{M}_\mathbf{i})\; p(\mathcal{M}_i) \tag{A.8}$$

If we assume that all parameterizations $\mathcal{M}_i$ share an equal prior probability, we can see from the previous equation that the posterior distribution only depends on the individual marginal likelihoods $p(\mathbf{d_{obs}}|\mathcal{M}_\mathbf{i})$. If we consider that there is no prior information, and the number of observations is large enough, we can define the Bayesian Information Criterion (BIC) Bishop (2006) as:

$$\begin{aligned} BIC(\mathcal{M}_i) &= -2\ln p(\mathbf{d_{obs}}|\mathcal{M}_\mathbf{i}) \\ &= M \ln N - 2\ \ln p(\mathbf{d_{obs}}|\tilde{\mathbf{m}}_\mathbf{i}, \mathcal{M}_\mathbf{i}). \end{aligned} \tag{A.9}$$

And the Akaike Information Criterion (AIC) as:

$$AIC(\mathcal{M}_i) = 2M - 2\ \ln p(\mathbf{d_{obs}}|\tilde{\mathbf{m}}_\mathbf{i}, \mathcal{M}_\mathbf{i}), \tag{A.10}$$

where N is the number of observations, M the number of parameters, and $\tilde{\mathbf{m}}_\mathbf{i}$ the maximum a posterior models corresponding parameters. These criteria allow us to choose between models taking into account the model complexity and the misfit in observations. The logarithmic term in equations A.5 and A.6 represents the capability of models to fit the observations. On the other hand, the first term corresponds to an ”Occam factor” in charge of penalizing the model complexity. Therefore, when we compare two different models, we will prefer the one with the lowest BIC and AIC.

APPENDIX B: SUPPLEMENTARY FIGURES

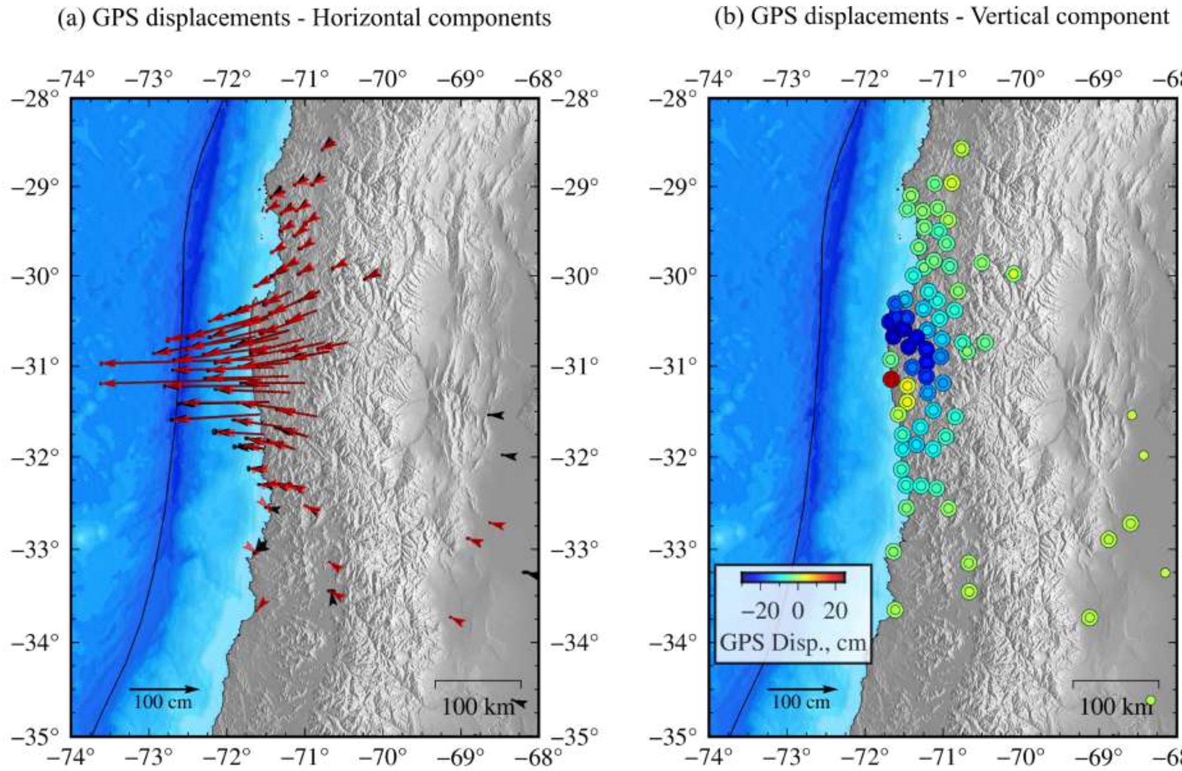

Figure A1. (a) Comparison between uncorrected (black arrows) horizontal displacement GPS and corrected from post-seismic displacement (red arrows). (b) Comparison between uncorrected (inner circle) vertical displacement GPS and corrected from post-seismic displacement (outer circle). The colormap indicates vertical component displacements.

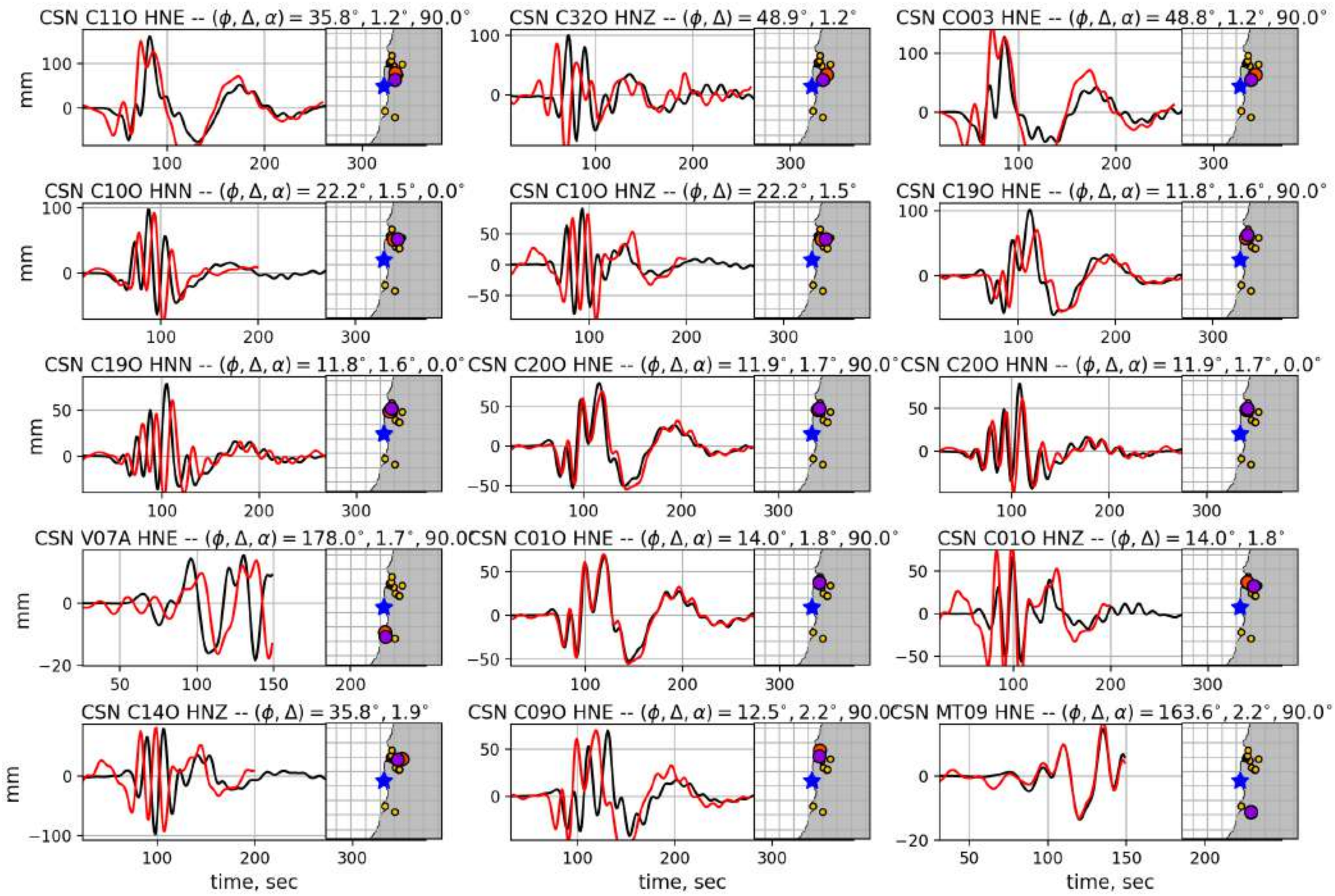

Figure A2. Comparison between displacements corrected from strong motion records and HRGPS displacements. Red and black waveforms represent HRGPS and strong motion, respectively. On the maps, the blue star represents the CSN hypocenter while circles indicate station location (orange for the strong motion station depicted, yellow for the ensemble of strong motion stations, and purple for HRGPS stations). ϕ, and Δ represent the azimuth and distance from the epicenter. α is the component azimuth (0° -north, 90° -east). Time-shifts between waveforms are due to slight differences in station location (i.e., between HRGPS and strong motion records).

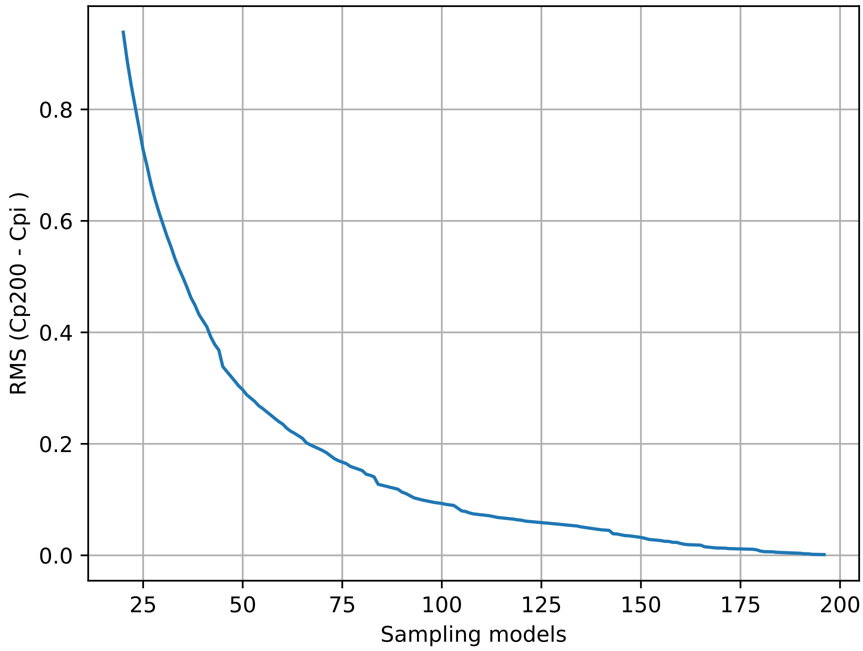

Figure A3. Difference between final empirical covariance matrix and intermediate covariance matrix calculated using a number of sampling models. The RMS is calculated using all the covariance matrix elements.

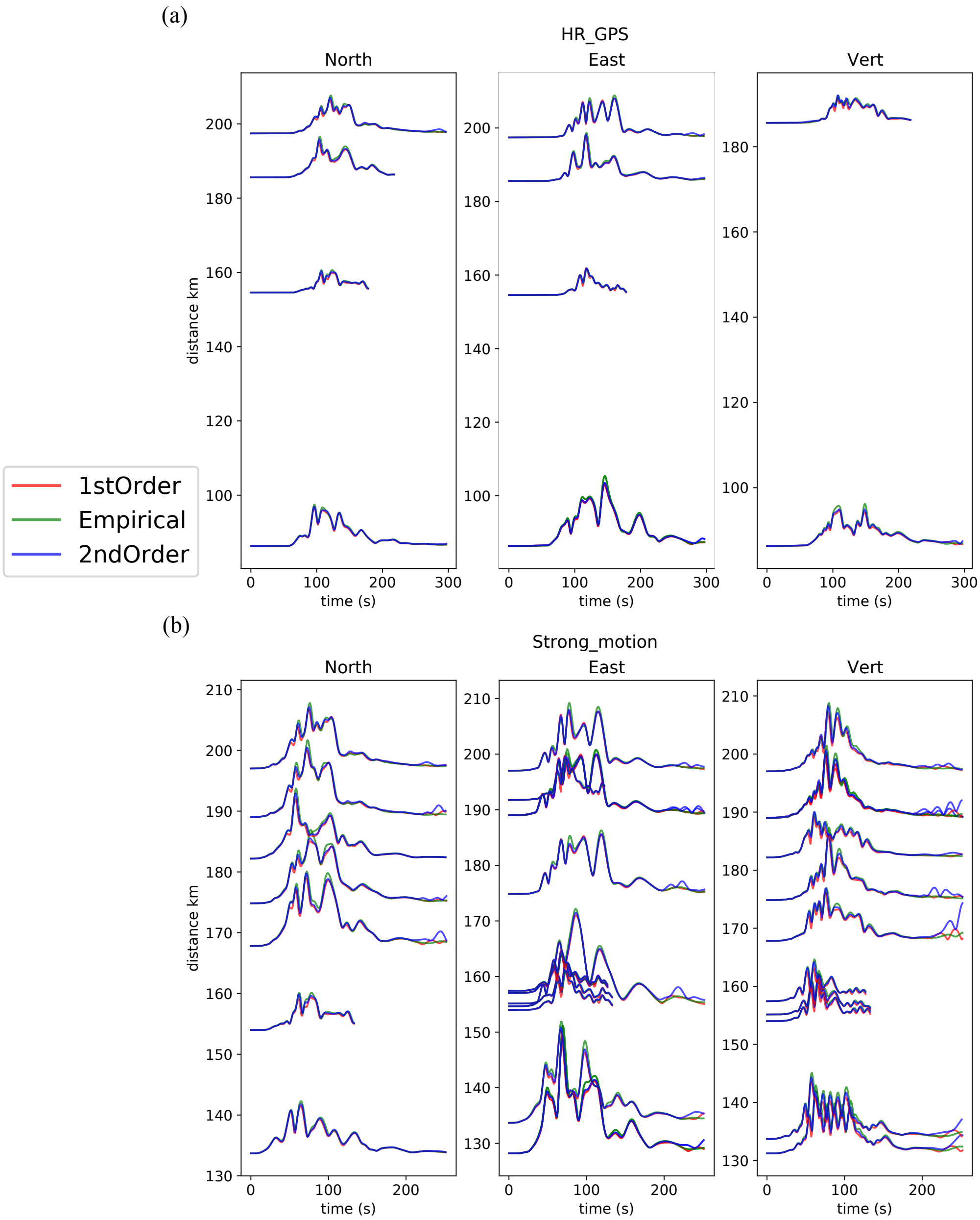

Figure A4. Covariance matrix comparison for HRGPS records (a) and strong Motion stations (b) at hypocenter distances $<$ 200 km. The green line represents the diagonal of the empirical covariance matrix (i.e., the matrix created from an ensemble of models). The red and blue line represents the diagonal of the matrix calculated using the 1st and 2nd order approximation approach.

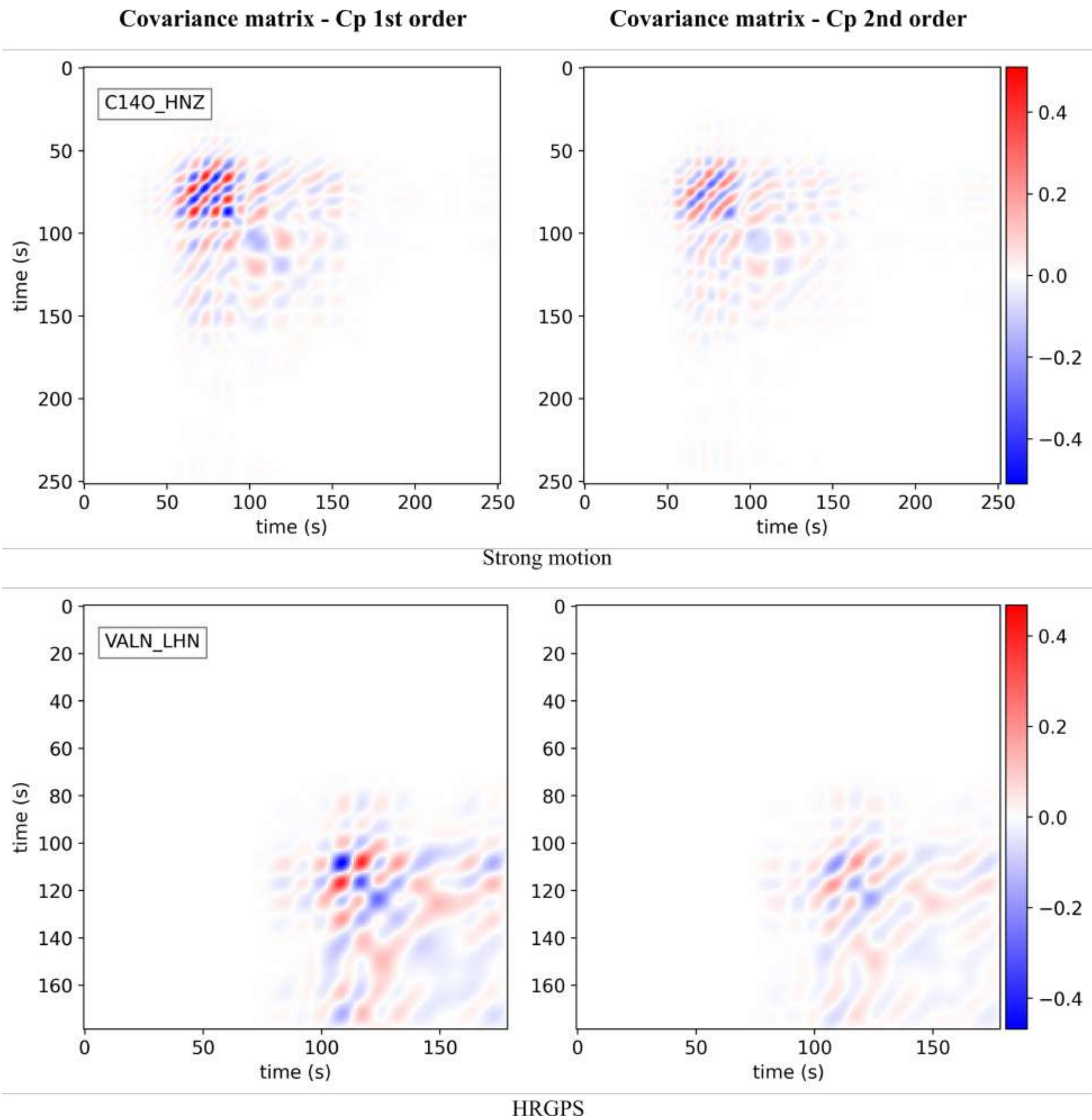

Figure A5. Comparison between strong motion (top) and HRGPS (bottom) covariance matrices calculated with the first order (left columns) and the second order (right columns) approximation approach. The colormap represents the difference between 1st/2nd order $\mathbf{C_p}$ and the empirical $\mathbf{C_p}$, normalized by the corresponding absolute maximum of the empirical $\mathbf{C_p}$.

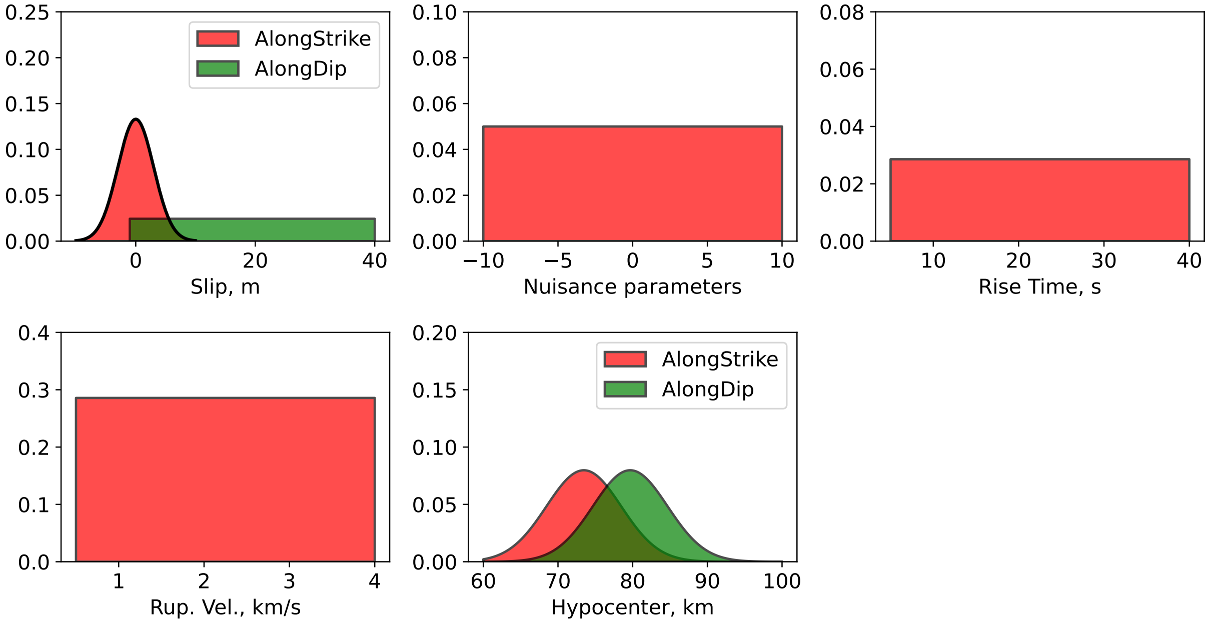

Figure A6. *A priori* probability density function (PDF) distributions for the inverted parameters. We add nuisance parameters to account for possible errors such as those caused by ionosphere in InSAR data (i.e., a constant offset for each image), and translation parameters for each GPS data set.

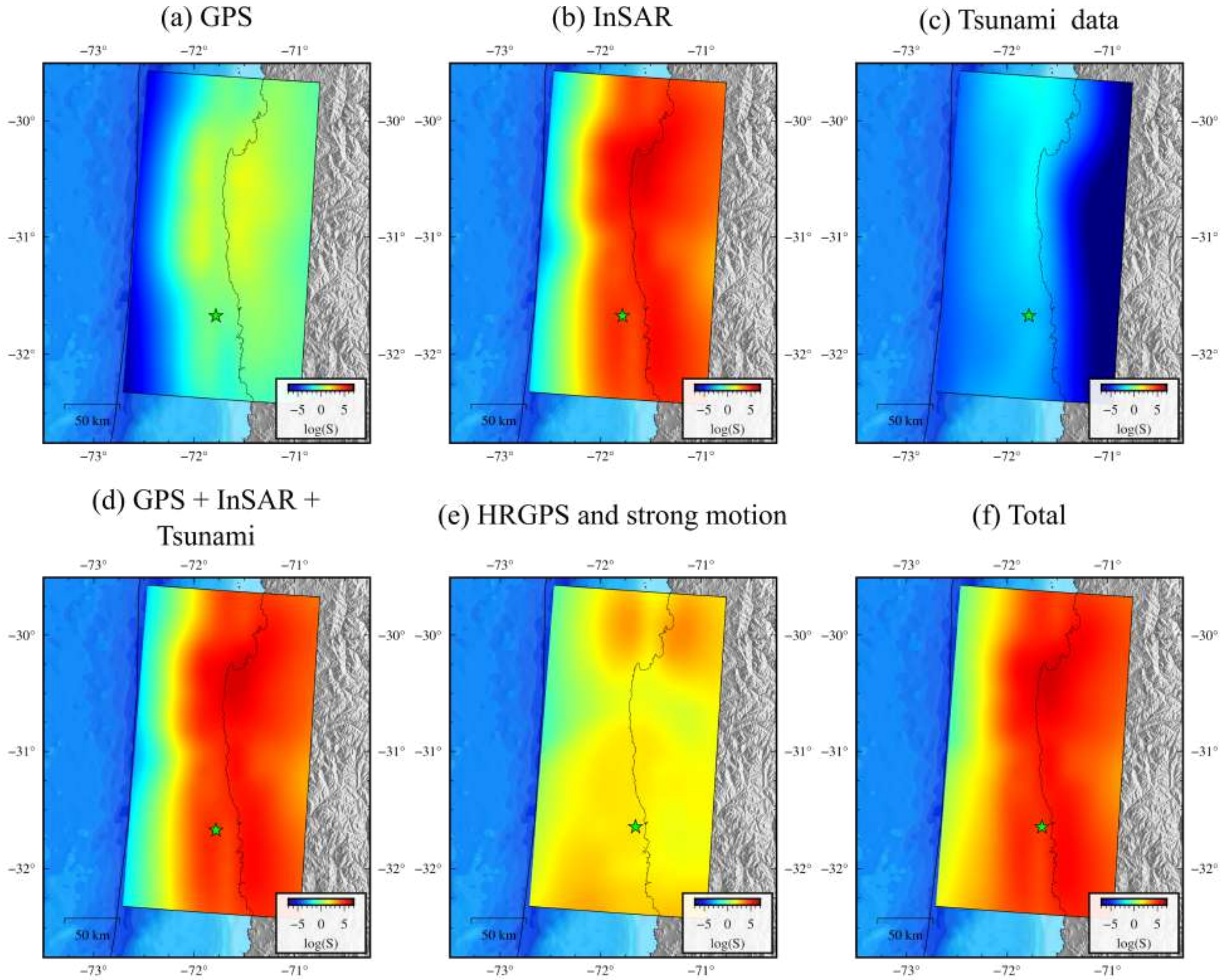

Figure A7. Sensitivity for each data set. The sensitivity is shown for (a) GPS, (b) InSAR, (c) tsunami data, (d) tsunami, InSAR, and GPS, (e) high rate GPS and strong motion, and (f) the ensemble of all data sets. /mThe sensitivity corresponds to a theoretical response given a one meter slip in each sub-fault.

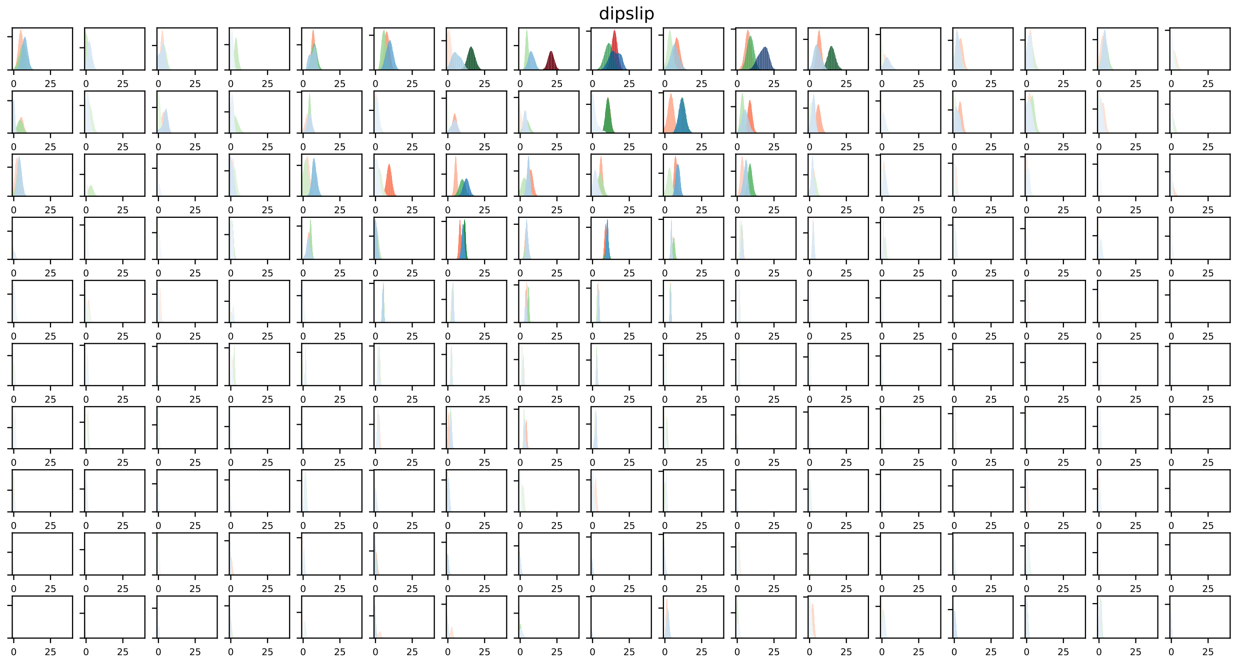

Figure A8. Posterior mean distributions for the dip slip parameters for various covariance matrices. The colors indicate which covariance matrix is used: the empirical Cp matrix (green), the first order approximation matrix (red), and the second order approximation matrix (blue). The strength of the colors are proportional to the magnitude of the slip.

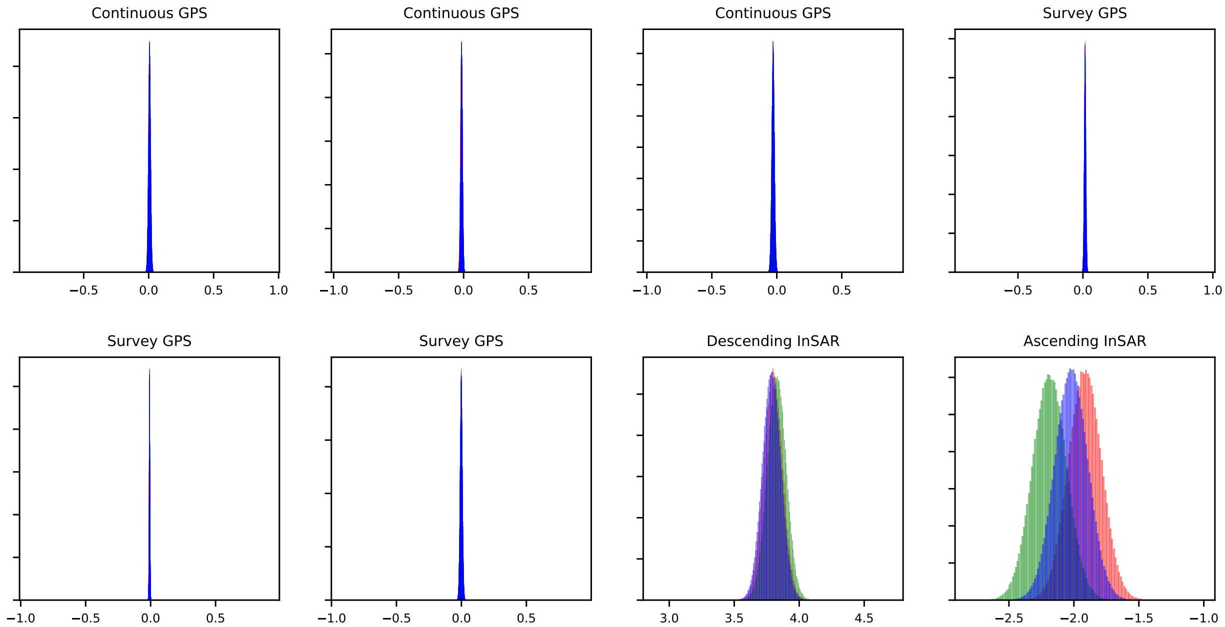

Figure A9. Posterior mean distributions for the nuisance parameters for various covariance matrices and different data sets. The colors indicate the empirical Cp matrix (green), the first order approximation matrix (red), and the second order approximation matrix (blue).

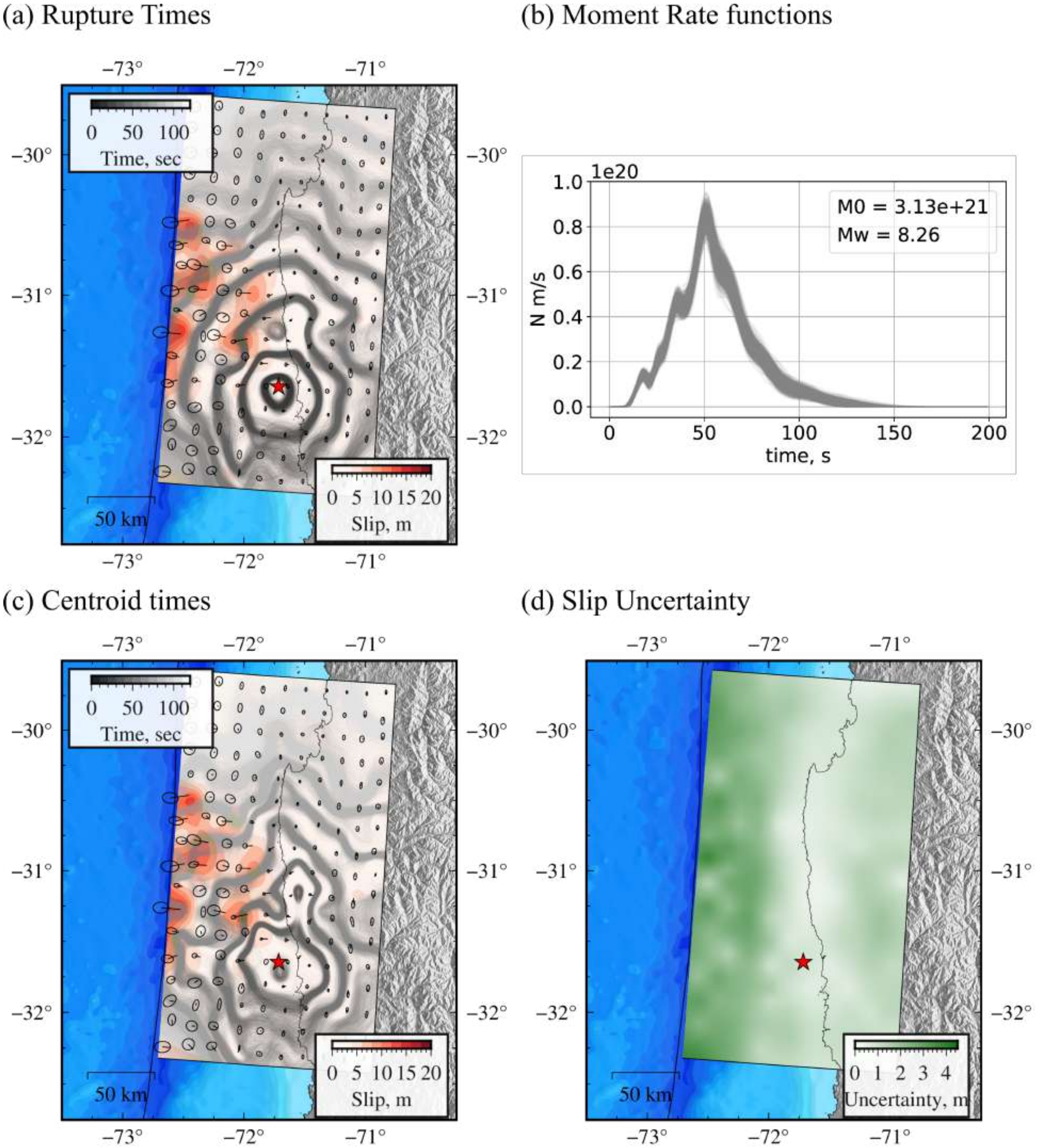

Figure A10. Impact of using an empirical covariance matrix $\mathbf{C_p}$ in slip inversion. (a) Posterior mean coseismic slip model, arrows represent the slip directions and the ellipses their uncertainties. Contours show stochastic rupture fronts samples from the *a posteriori* distribution every 10 seconds. (b) Stochastic moment rate functions. (c) Posterior mean coseismic slip model with contours that represent stochastic centroid time fronts samples from the *a posteriori* distribution. (d) Uncertainty of the ensemble of coseismic slip models. The red star in the figures represents the inverted hypocenter location.

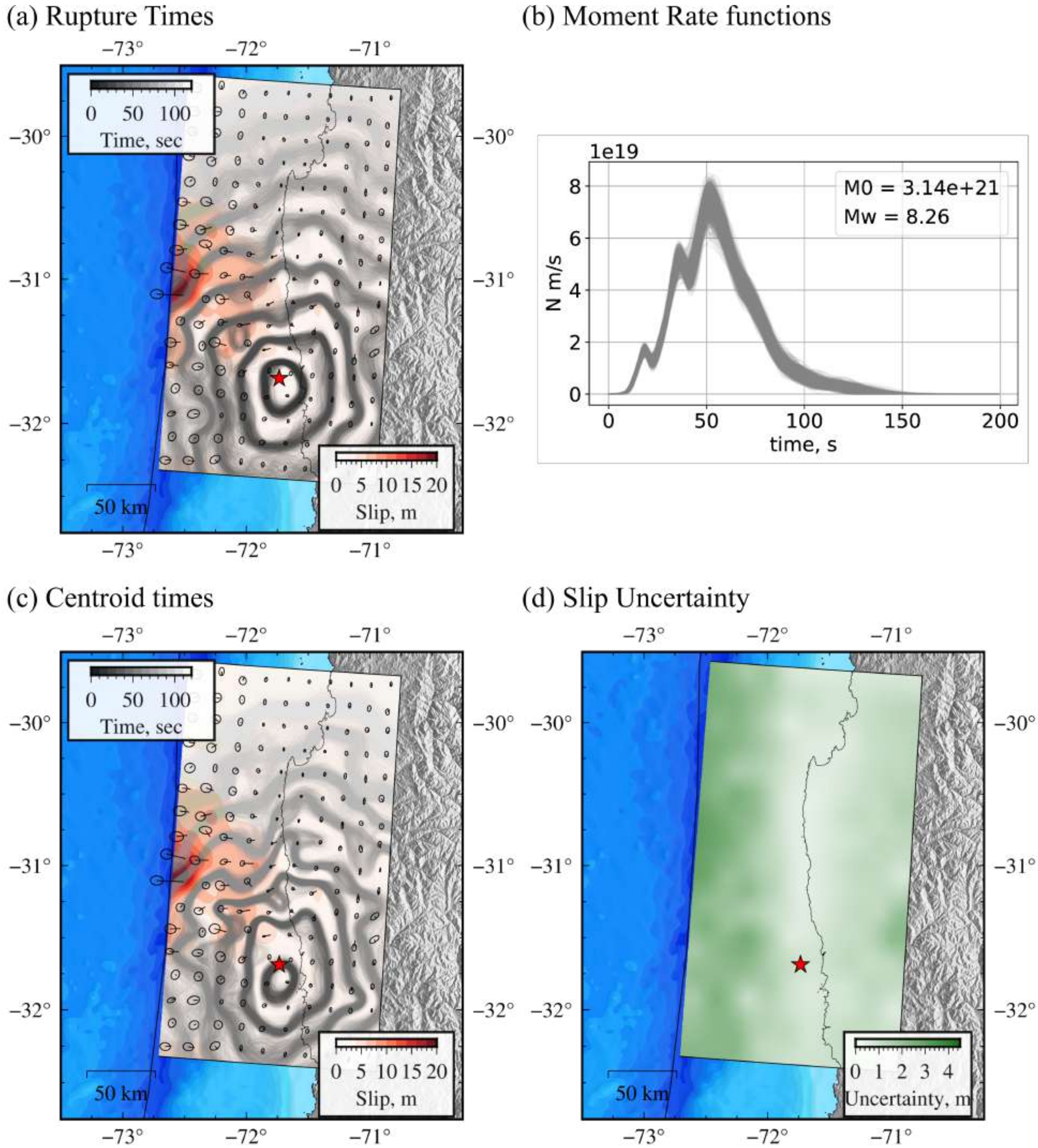

Figure A11. Impact of using a 1st order approximation $\mathbf{C_p}$ in slip inversion. (a) Posterior mean coseismic slip model, arrows represent the slip directions and the ellipses their uncertainties. Contours show stochastic rupture fronts samples from the *a posteriori* distribution every 10 seconds. (b) Stochastic moment rate functions. (c) Posterior mean coseismic slip model with contours that represent stochastic centroid time fronts samples from the *a posteriori* distribution. (d) Uncertainty of the ensemble of coseismic slip models. The red star in the figures represents the inverted hypocenter location.

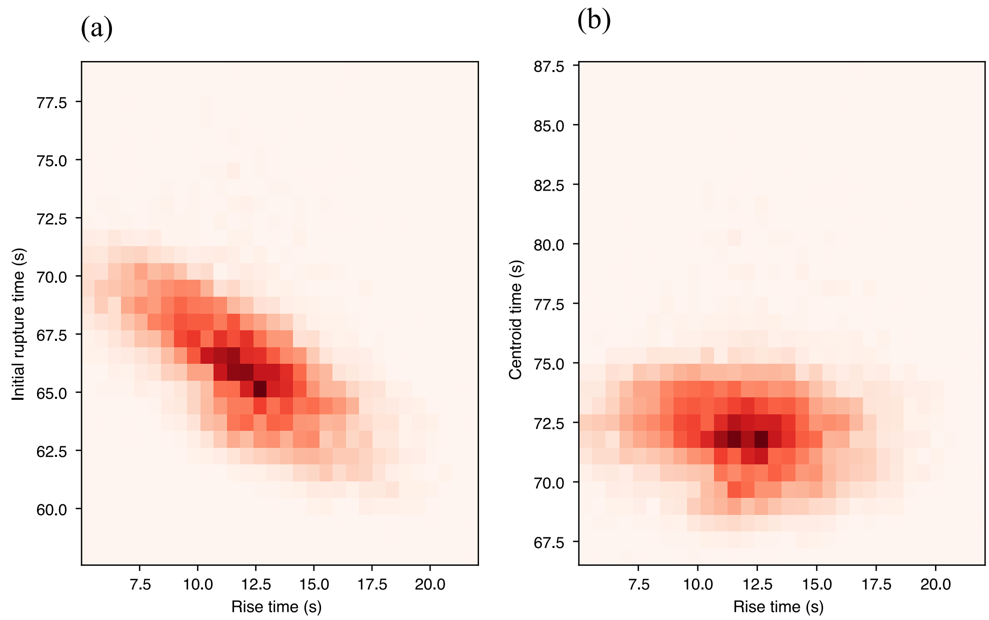

Figure A12. Comparison between rupture and rise times (a) and slip pulse centroid and rise times (b) for the patch with maximum slip. This subfault is located at the shallowest part of the fault geometry.

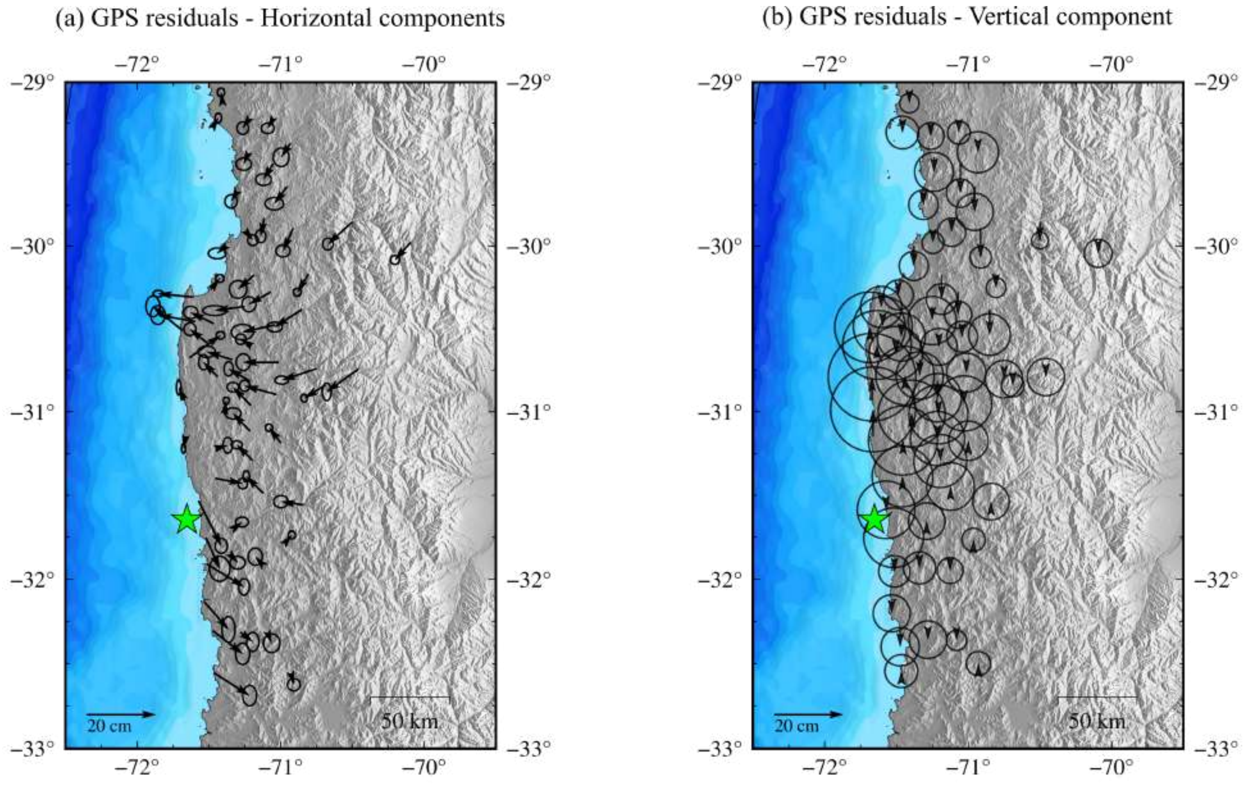

Figure A13. (a) Residuals for observed horizontal GPS and predictions for the posterior mean model using a 2nd order approximation $\mathbf{C_p}$. (b) Residuals for observed vertical GPS and predictions for the posterior mean model using a 2nd order approximation. Ellipses correspond to observational uncertainties plus forward model uncertainties.

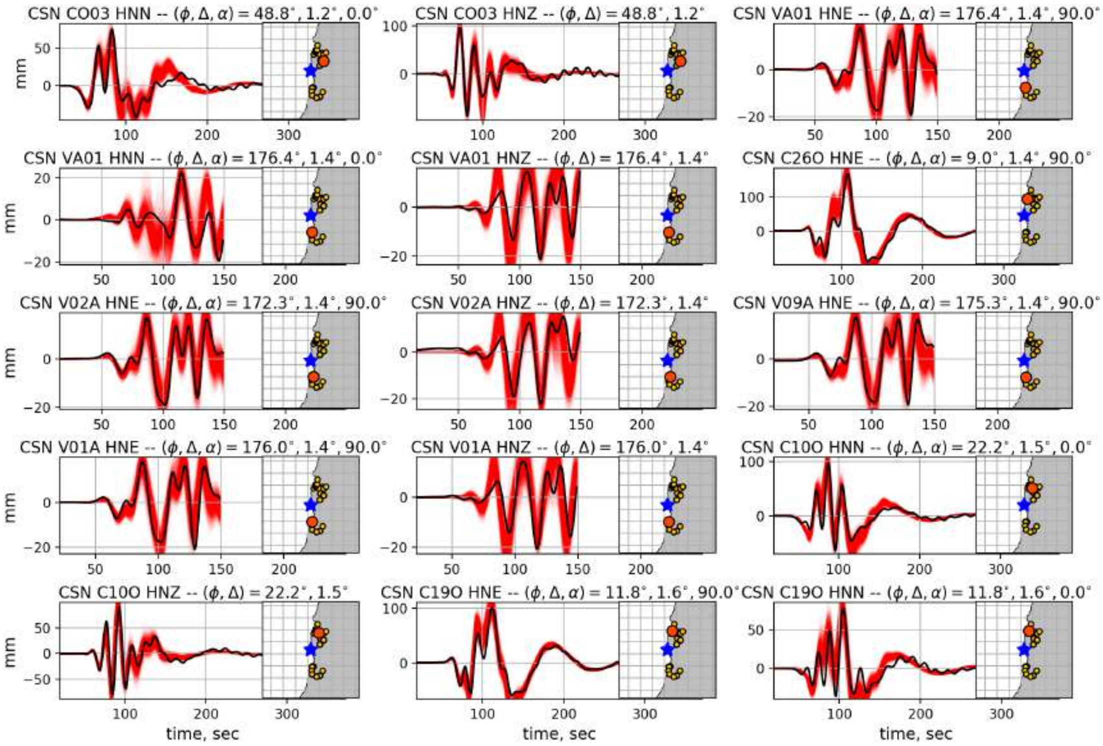
CSN CO03 HNN -- $(\phi, \Delta, \alpha) = 48.8^\circ, 1.2^\circ, 0.0^\circ$
CSN CO03 HNZ -- $(\phi, \Delta) = 48.8^\circ, 1.2^\circ$
CSN VA01 HNE -- $(\phi, \Delta, \alpha) = 176.4^\circ, 1.4^\circ, 90.0^\circ$
CSN VA01 HNN -- $(\phi, \Delta, \alpha) = 176.4^\circ, 1.4^\circ, 0.0^\circ$
CSN VA01 HNZ -- $(\phi, \Delta) = 176.4^\circ, 1.4^\circ$
CSN C26O HNE -- $(\phi, \Delta, \alpha) = 9.0^\circ, 1.4^\circ, 90.0^\circ$
CSN V02A HNE -- $(\phi, \Delta, \alpha) = 172.3^\circ, 1.4^\circ, 90.0^\circ$
CSN V02A HNZ -- $(\phi, \Delta) = 172.3^\circ, 1.4^\circ$
CSN V09A HNE -- $(\phi, \Delta, \alpha) = 175.3^\circ, 1.4^\circ, 90.0^\circ$
CSN V01A HNE -- $(\phi, \Delta, \alpha) = 176.0^\circ, 1.4^\circ, 90.0^\circ$
CSN V01A HNZ -- $(\phi, \Delta) = 176.0^\circ, 1.4^\circ$
CSN C10O HNN -- $(\phi, \Delta, \alpha) = 22.2^\circ, 1.5^\circ, 0.0^\circ$
CSN C10O HNZ -- $(\phi, \Delta) = 22.2^\circ, 1.5^\circ$
CSN C19O HNE -- $(\phi, \Delta, \alpha) = 11.8^\circ, 1.6^\circ, 90.0^\circ$
CSN C19O HNN -- $(\phi, \Delta, \alpha) = 11.8^\circ, 1.6^\circ, 0.0^\circ$
mm
time, sec

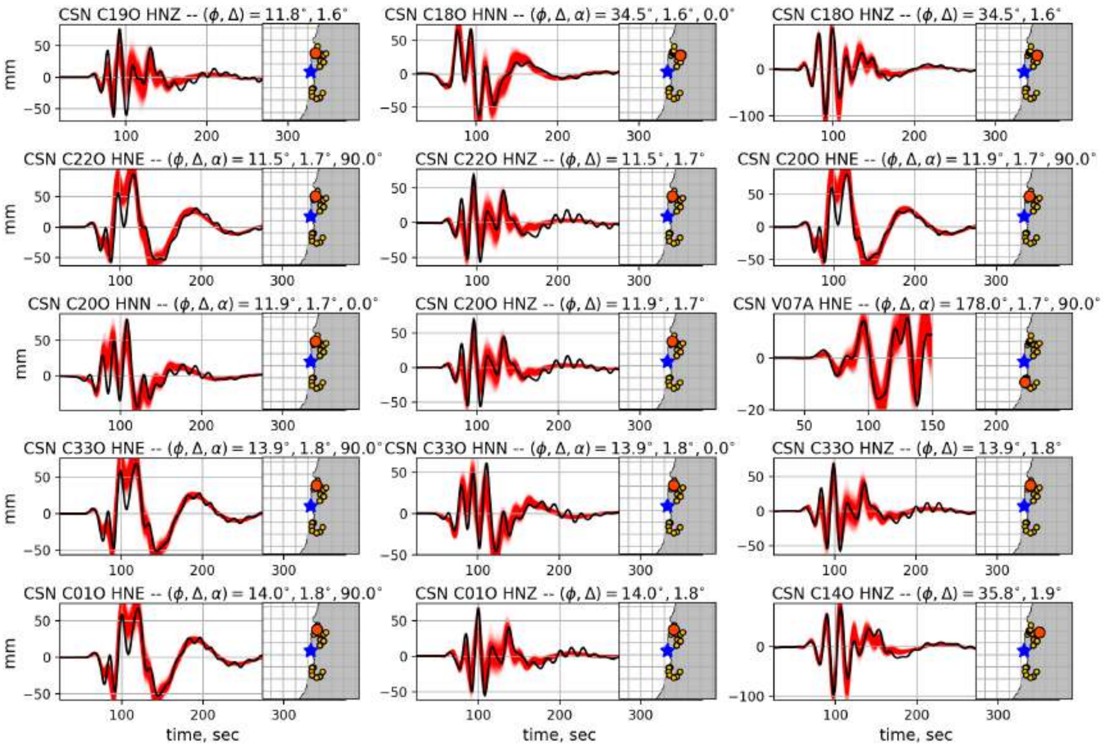
CSN C19O HNZ -- $(\phi, \Delta) = 11.8^\circ, 1.6^\circ$
CSN C18O HNN -- $(\phi, \Delta, \alpha) = 34.5^\circ, 1.6^\circ, 0.0^\circ$
CSN C18O HNZ -- $(\phi, \Delta) = 34.5^\circ, 1.6^\circ$
CSN C22O HNE -- $(\phi, \Delta, \alpha) = 11.5^\circ, 1.7^\circ, 90.0^\circ$
CSN C22O HNZ -- $(\phi, \Delta) = 11.5^\circ, 1.7^\circ$
CSN C20O HNE -- $(\phi, \Delta, \alpha) = 11.9^\circ, 1.7^\circ, 90.0^\circ$
CSN C20O HNN -- $(\phi, \Delta, \alpha) = 11.9^\circ, 1.7^\circ, 0.0^\circ$
CSN C20O HNZ -- $(\phi, \Delta) = 11.9^\circ, 1.7^\circ$
CSN V07A HNE -- $(\phi, \Delta, \alpha) = 178.0^\circ, 1.7^\circ, 90.0^\circ$
CSN C33O HNE -- $(\phi, \Delta, \alpha) = 13.9^\circ, 1.8^\circ, 90.0^\circ$
CSN C33O HNN -- $(\phi, \Delta, \alpha) = 13.9^\circ, 1.8^\circ, 0.0^\circ$
CSN C33O HNZ -- $(\phi, \Delta) = 13.9^\circ, 1.8^\circ$
CSN C01O HNE -- $(\phi, \Delta, \alpha) = 14.0^\circ, 1.8^\circ, 90.0^\circ$
CSN C01O HNZ -- $(\phi, \Delta) = 14.0^\circ, 1.8^\circ$
CSN C14O HNZ -- $(\phi, \Delta) = 35.8^\circ, 1.9^\circ$
mm
time, sec

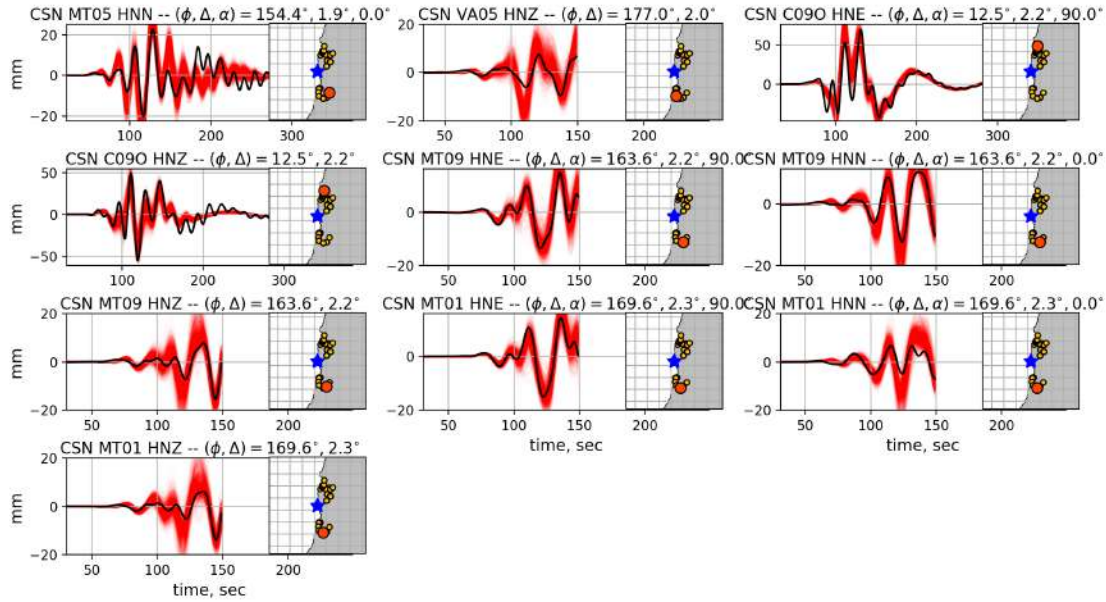

Figure A14. Examples of comparisons between data (black) and stochastic predictions (red) for HRGPS and strong motion stations using a 2nd order approximation $\mathbf{C_p}$. On the maps, the blue star represents the hypocenter while circles indicate station location (orange for the station depicted and yellow for the other stations).

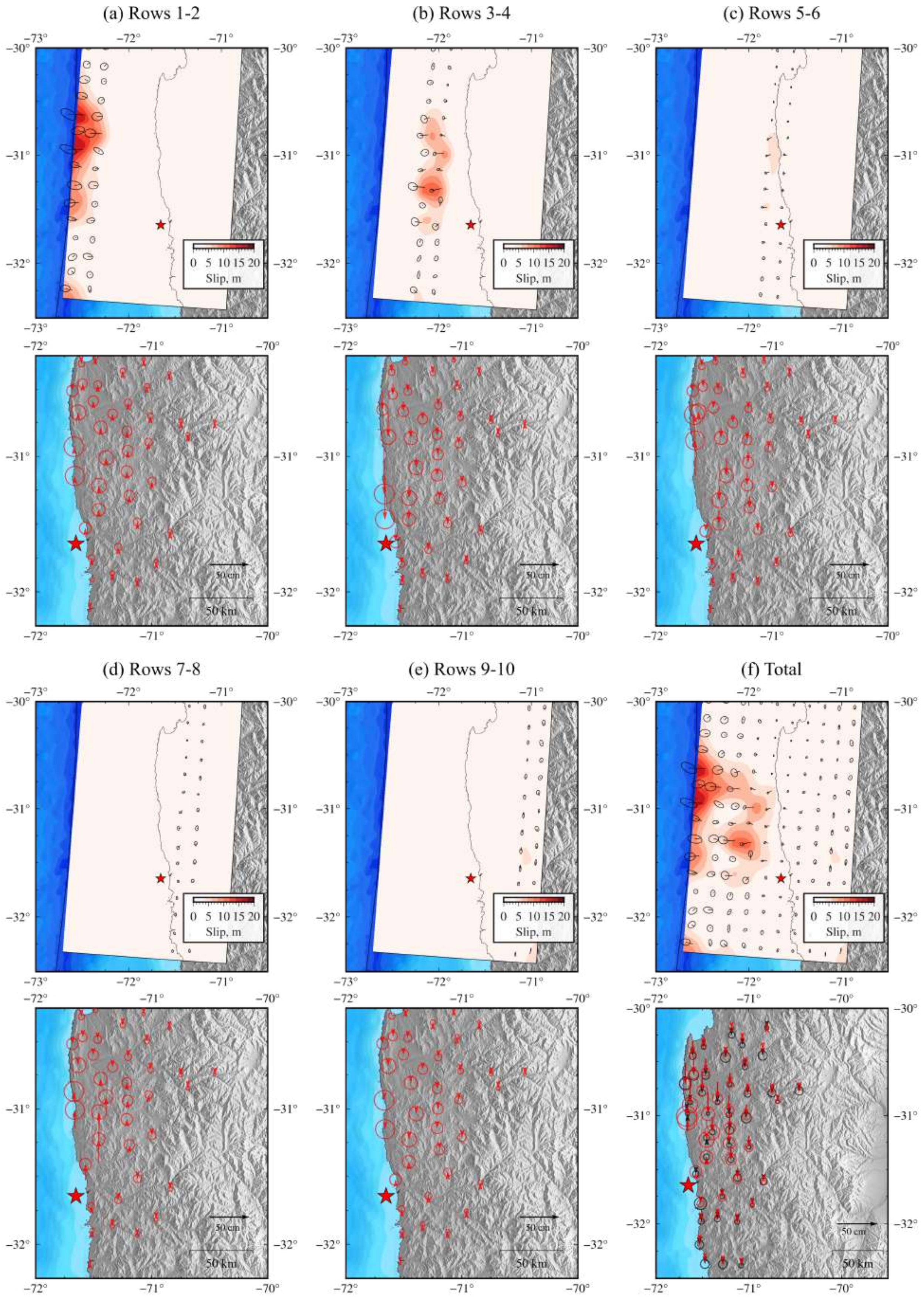

Figure A15. Vertical displacement predictions for the posterior mean model (red arrows) calculated for different subfault slips (a-e) and total displacement (f). The observed vertical GPS (black arrow) is show in (f).

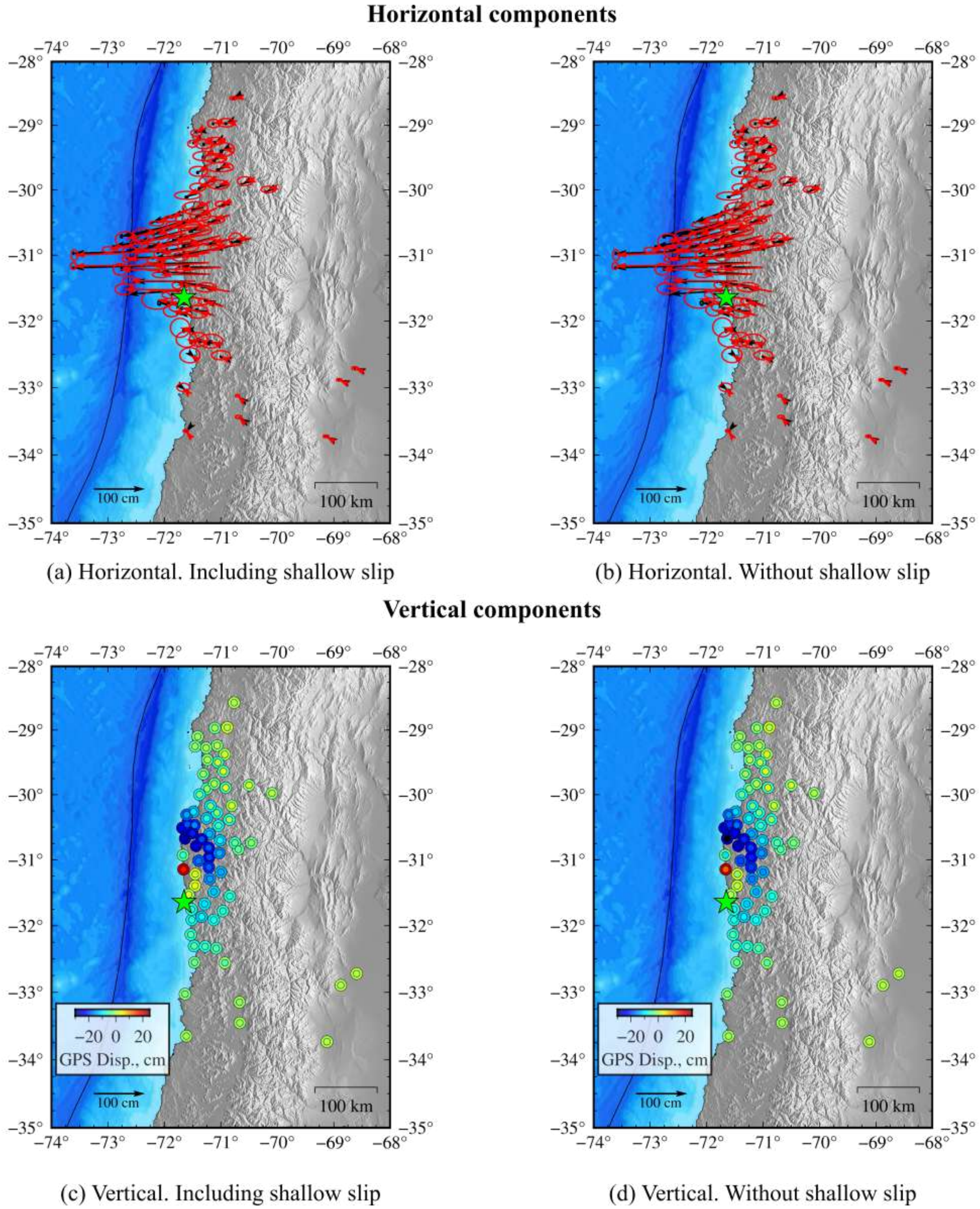

Figure A16. Comparison between models with shallow slip and imposing a zero slip at shallow depth. Observed horizontal GPS (black arrows) and predictions for the posterior mean model (red arrows) using a 2nd order approximation $\mathbf{C_p}$ including shallow slip (a) and without shallow slip (b). Observed vertical GPS (outer circle) and predictions for the posterior mean model (inner circle) including a shallow slip (c) and without shallow slip (d). The colormap indicates the corresponding vertical displacements.

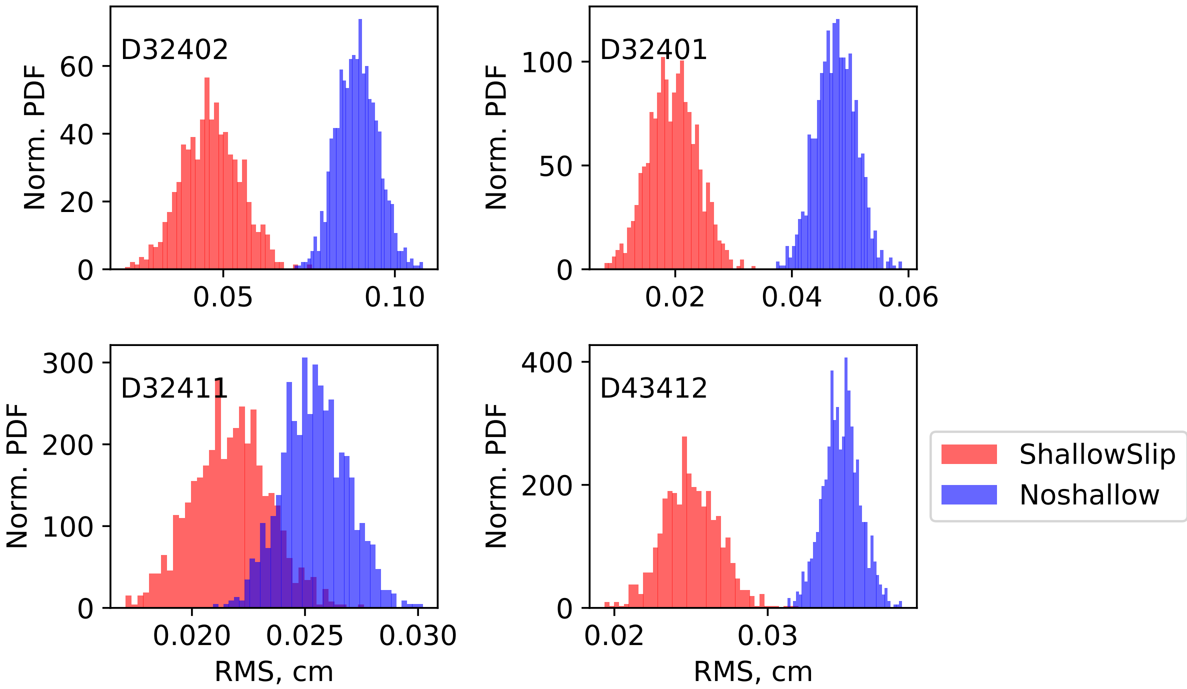

Figure A17. Comparison of RMS distribution between tsunami observations and stochastic predictions with shallow slip (red) and without shallow slip (blue) for four selected stations.

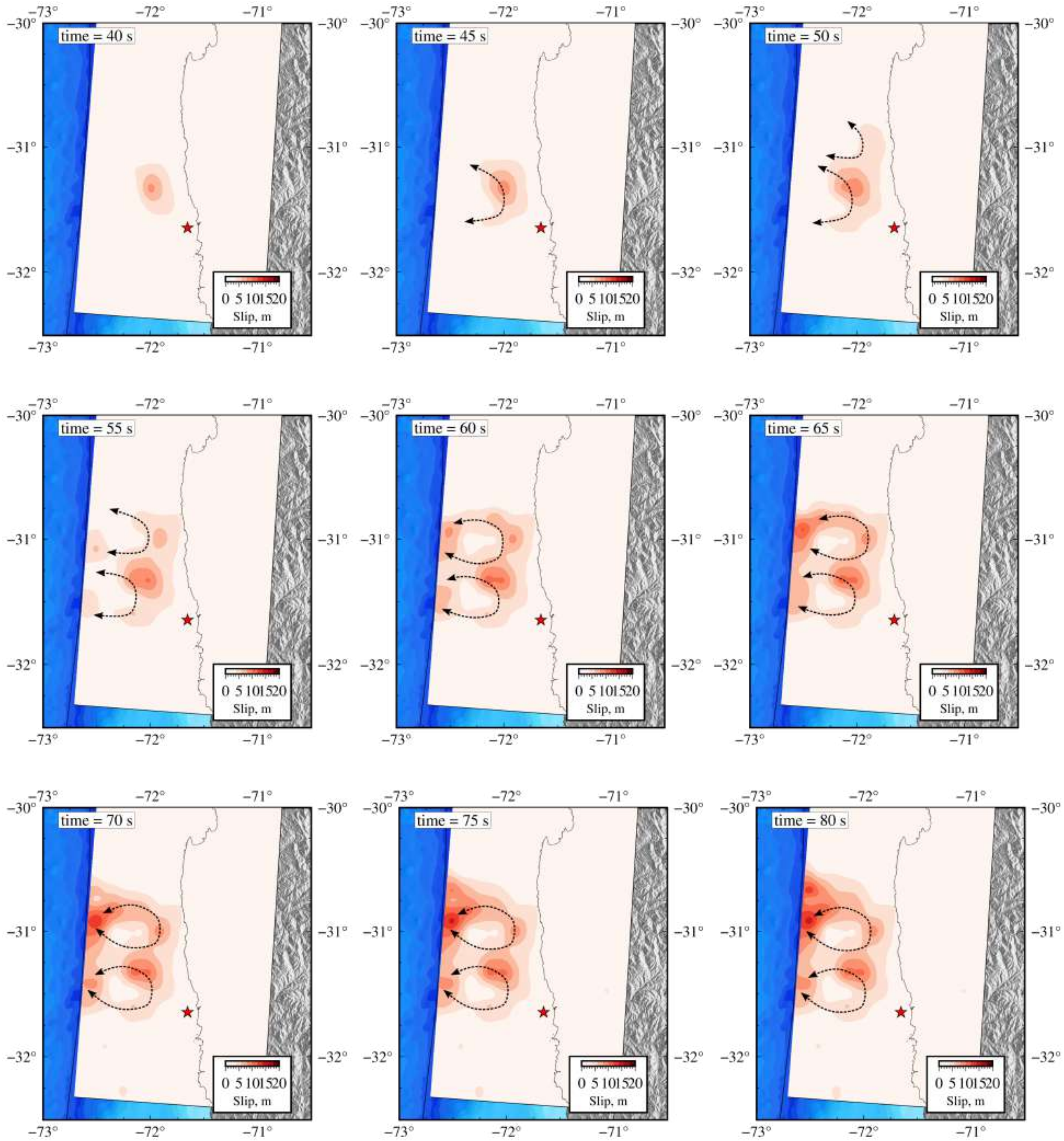

Figure A18. Five seconds snapshots of slip evolution. Slip is calculated using the posterior mean coseismic model using the 2nd order $\mathbf{C_P}$ solution. The red star is the inverted hypocenter location. Arrow lines represent the possible encircled locations.

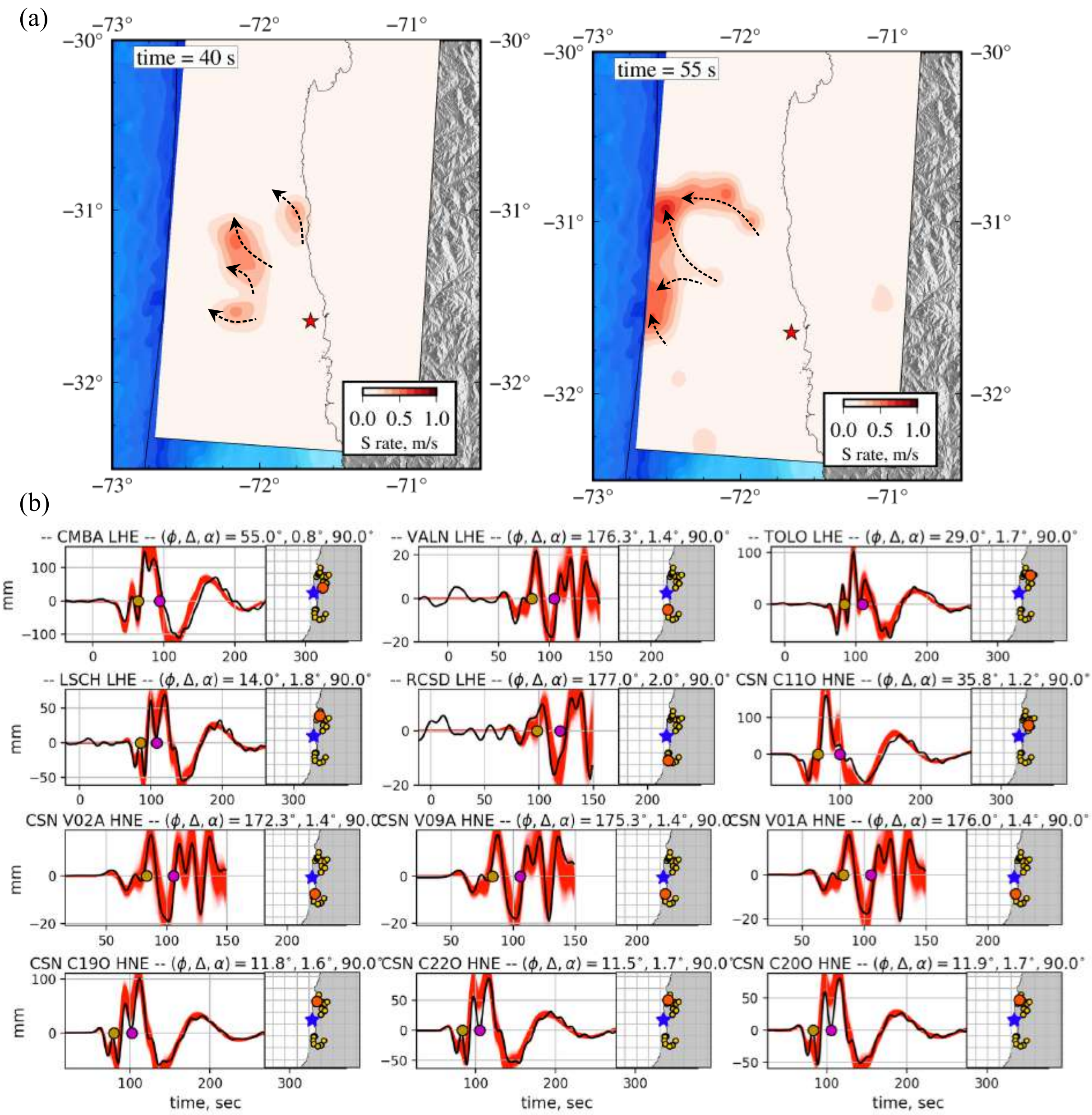

Figure A19. (a) Slip rate snapshots at the beginning of the south west encircling effect (left) at 40 seconds, and at the end of the encircling (right) at 55 seconds. This south-west encircling effect began at 35 seconds and starts finishing at 50 seconds. The slip rate was calculated as in Figure 16. The red star corresponds to the inverted hypocenter. (b) Examples of east observed and stochastic prediction waveforms with S wave theoretical arrival times that correspond to the start (gold) and end (purple) of the encircling effect. The other captions are similar to Figure A14.

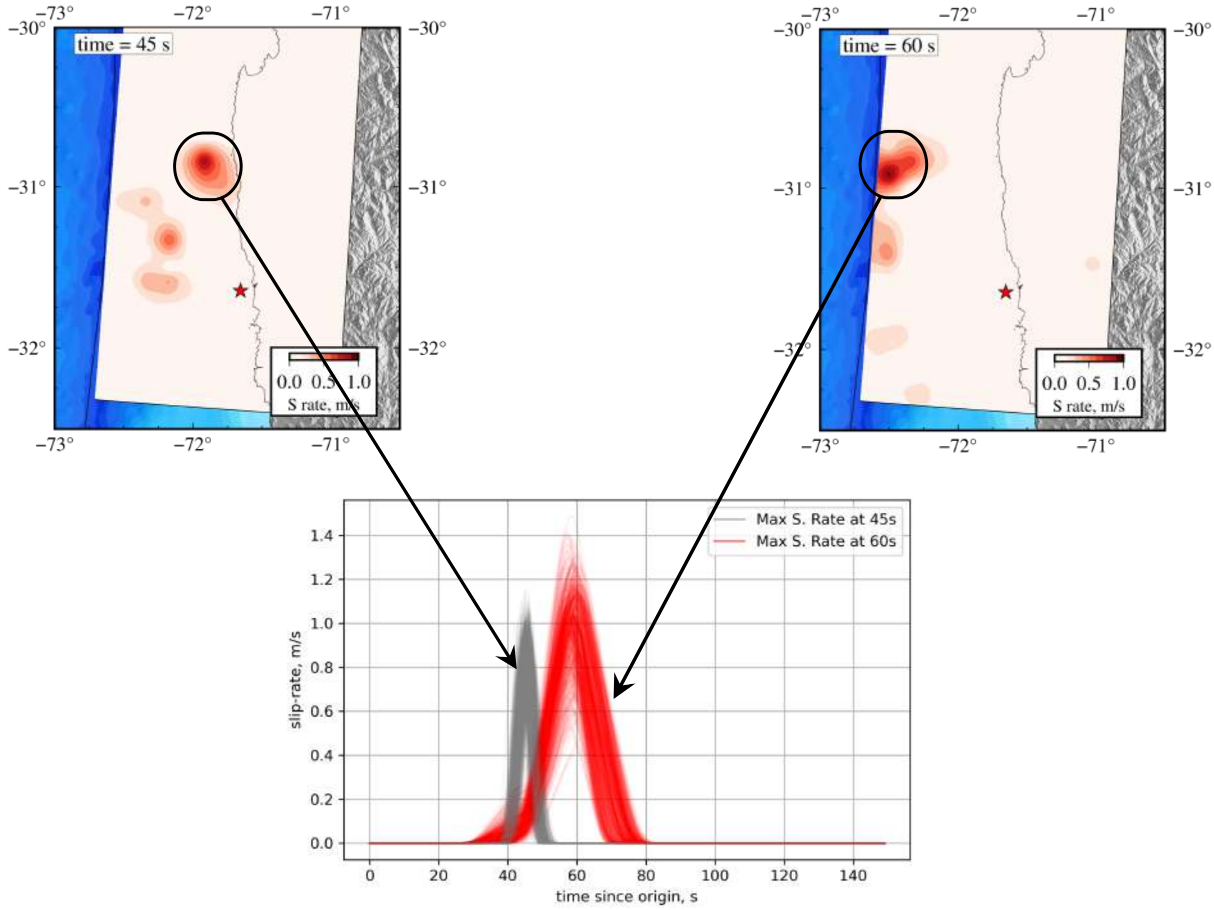

Figure A20. Stochastic posterior slip rate functions for regions with maximum slip rates at different times, at 45 seconds(gray) and 60 seconds (red). The corresponding regions are shown in the inset maps. The red star corresponds to the inverted hypocenter.

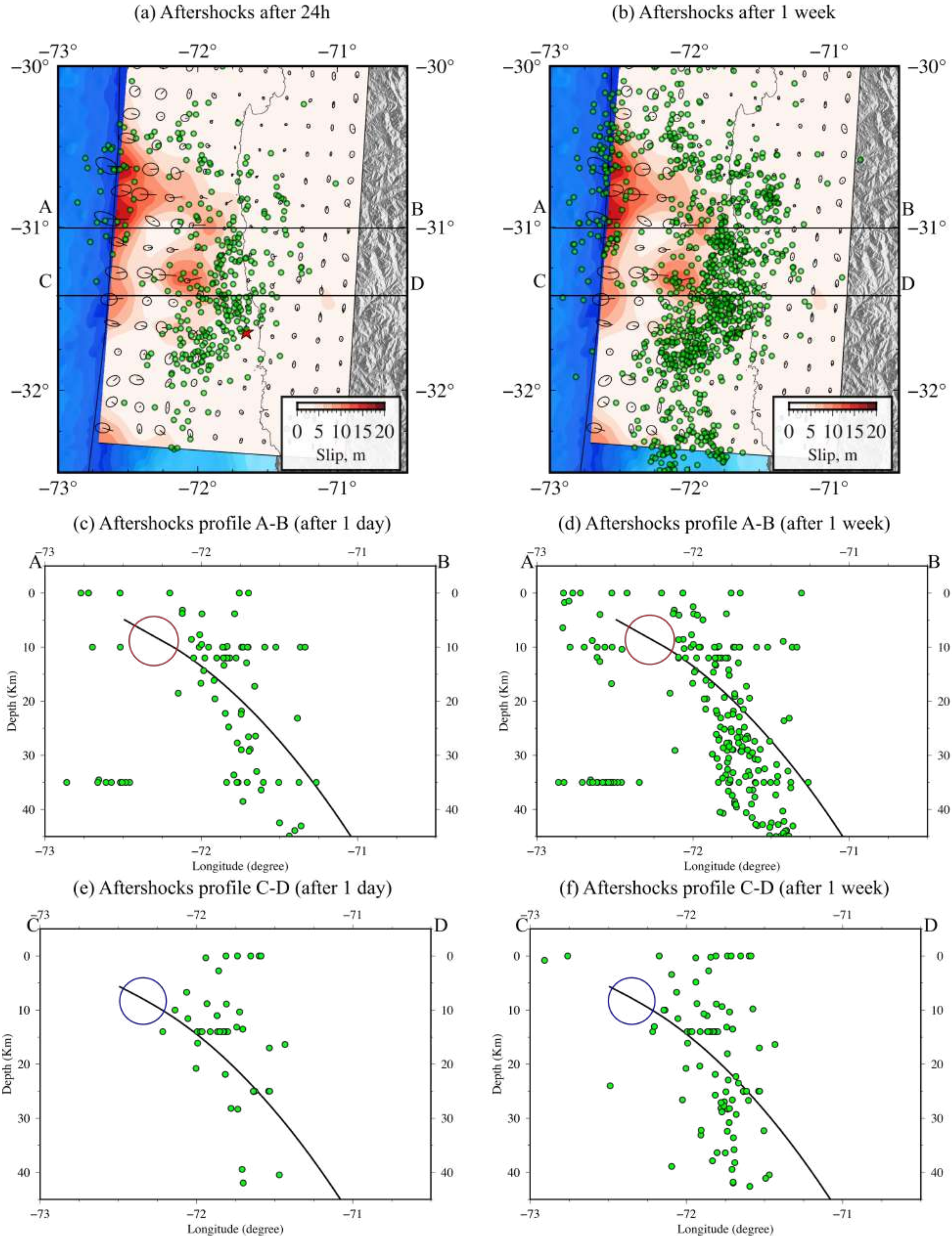

Figure A21. Posterior coseismic mean model with ISC aftershocks locations (green dots) after 24 hours (a), and one week after the mainshock (b) with their corresponding depth profile for the A-B profile (c-d) and the C-D profile (e-f). The black line corresponds to the fault geometry used in this study. The red and blue circles correspond to the encircled regions, respectively.